1998

An empirical model of the tidal currents in the Gulf of Farallones

Steger, John M.

Deep-Sea Research II, Volume 45, (1998), pp. 1471-1505
http://hdl.handle.net/10945/43239

PERGAMON

Deep-Sea Research II 45 (1998) 1471–1505

DEEP-SEA RESEARCH
PART II

An empirical model of the tidal currents in the Gulf of the Farallones

John M. Steger[a,*], Curtis A. Collins[b], Franklin B. Schwing[a], Marlene Noble[c], Newell Garfield[b], Marc T. Steiner[b]

[a]*NOAA/NMFS Pacific Fisheries Environmental Laboratory, Pacific Grove, CA, USA*
[b]*Naval Postgraduate School, Monterey, CA, USA*
[c]*USGS, Menlo Park, CA, USA*

Received 18 April 1997; received in revised form 1 December 1997; accepted 4 December 1997

Abstract

Candela et al. (1990, 1992) showed that tides in an open ocean region can be resolved using velocity data from a ship-mounted ADCP. We use their method to build a spatially varying model of the tidal currents in the Gulf of the Farallones, an area of complicated bathymetry where the tidal velocities in some parts of the region are weak compared to the mean currents. We describe the tidal fields for the M_2, S_2, K_1, and O_1 constituents and show that this method is sensitive to the model parameters and the quantity of input data. In areas with complex bathymetry and tidal structures, a large amount of spatial data is needed to resolve the tides. A method of estimating the associated errors inherent in the model is described. Published by Elsevier Science Ltd.

1. Introduction

This paper describes a model of the tidal currents in the Gulf of the Farallones (Seaward of San Francisco Bay) that uses observations of ocean currents from moored current meters and ship-mounted acoustic Doppler current profilers (ADCPs) to predict tidal velocities that can be effectively subtracted from the raw ADCP data to reduce variance at tidal frequencies. The purpose of "detiding" the ADCP data is to study the subtidal seasonal circulation of the continental shelf and upper continental slope of the Gulf, a relatively little studied region of the central California coast, where initial analysis of ADCP data from five cruises in 1991–1992 suggested that tidal

*Corresponding author. Fax: 001 408 656 3686.

0967-0645/98/$–see front matter Published by Elsevier Science Ltd.
PII: S0967-0645(98)00040-X

velocities would complicate study of the lower frequency current signal (Ramp et al., 1995). However, in addition to detiding ADCP data, the model may be useful for other applications, such as evaluating the effect of tidal currents and tidal residual circulations on pollution transport, coastal engineering projects, distribution of fisheries, and marine navigation.

If measurements of currents in a region are available, empirical tidal models are quickly implemented since they require no prior knowledge of the currents or their physics. Unlike theoretical tidal models, complicated bathymetries or coastlines are not a problem and there is no need to predetermine boundary conditions. This portability of the empirical method is attractive in situations where the tides need to be modeled rapidly, such as search and rescue, military operations, or environmental disasters.

Unlike velocity data from moored current meters, the tidal signal cannot be removed from ship-mounted ADCP data by low-pass filtering or simple harmonic analysis such as the methods of Foreman (1978). This is because, in most cases, the amplitude and phase of the tidal currents vary with position and depth as well as time, and the tides are confounded with the varying non-tidal mesoscale circulations. These methods cannot distinguish between temporal and spatial variability and, in general, assume the variance in a current record is due to tidal variance. An extreme example of this would be the case of a ship repeatedly surveying a region of high velocity currents each night but in the daytime working in a nearby area with lower velocity or opposite currents. Instead of resolving the spatial variation, a diurnal tide would be incorrectly inferred.

There are several methods for removing tidal velocities from ship-mounted ADCP measurements. A high-resolution numerical tidal model was used by Foreman and Freeland (1991) to detide ADCP data off Vancouver Island. However, such a model does not currently exist for the Farallones region and the development of one was beyond the scope of the intent to study the subtidal circulation. Dowd and Thompson (1996) estimated tidal velocities by creating a simple barotropic tidal model of the Scotian Shelf and solving for the boundary conditions by fitting the model to ADCP observations. Tidal constituents can be estimated directly from ADCP data if the ship is stationary through at least one diurnal tidal cycle, repeatedly sails over the same tracks until a pseudo-stationary time series can be constructed (Geyer and Signell, 1990), or repeats its tracks four times in a diurnal period and the "diurnally averaged flow" is calculated (Katoh et al., 1996). However, this may be an inefficient use of shiptime. Another method would be to calculate the tidal constituent values at several concurrently deployed or historical current meter mooring sites and interpolate the tidal values throughout the region. This simplistic approach was used in the Gulf of the Farallones by Gezgin (1991), but probably does not adequately model the tidal fields given the spatial and temporal variability implied by the historical current meter records deployed in the Gulf. A final method of removing tidal data is to create a spatially dependent empirical tidal model using the ADCP data and all available current meter data. This method, first used by Candela et al. (1990, 1992) to remove tides from ADCP data collected in the Yellow Sea, extends the stationary time-series techniques of Foreman (1978) to solve for tides by fitting observations of currents to

spatially dependant functions of tidal frequency and solving using the method of least squares. The Candela method was later applied by Allen (1995) to the Iceland-Færœs Front.

The Candela method is used here to detide the Gulf of the Farallones data set. The technique has been extended to include a vastly larger data set (over 700,000 current meter and ADCP observations compared to Candela et al.'s (1990, 1992) use of 129 ADCP observations) and to include depth as a variable in the tidal model to incorporate the effects of baroclinic tides. These extensions are necessary because an inherent characteristic of the method is that in fitting the data to the specified tidal frequencies using least squares the strongest signals in the data are emphasized. Since the mean flow in the Gulf of the Farallones is much stronger than the tidal currents, relatively few observations are necessary in the Gulf to resolve the mean currents, but a large number of observations is required to discriminate the tidal fields from the mean.

An advantage of having a large data set is that as longer time series are used to create the model, the Rayleigh criterion (Godin, 1972) is met for more closely spaced tidal frequencies. For instance, Foreman and Freeland (1991) applied the Candela method to only three days of data and could only determine a "lumped M_2 and K_1"; i.e., a single semi-diurnal and a single diurnal frequency that included all the energy in those bands. Although additional semi-diurnal and diurnal frequencies could be estimated by inference using standard ratios or ratios determined from local sea level stations or a long current meter data series, a more accurate method is to use longer periods of observations if available. This is particularly important in areas such as the Gulf of the Farallones where the ratios may varying spatially and the local sea level ratios may not reflect local tidal current ratios. We have used our model to examine the M_2 (12.4 h), S_2 (12.0 h), K_1 (23.9 h), and O_1 (25.8 h) tidal constituents that sea level data show account for most of the tidal variability in the Gulf (Noble and Gelfenbaum, 1990).

In Section 2 we describe the unique bathymetric and topographic characteristics of the Gulf and review the historical tidal observations there. In Section 3 the ADCP and current meter data used in the model are detailed. In section 4 the Candela model and our extensions are explained. In Section 5 we describe several tidal models for the Gulf applying the empirical method to observational data sets of varying sizes and sources. In Section 6 we discuss the limitations of the method and a means of determining the associated errors.

2. The Gulf of the Farallones

The Gulf of the Farallones (Fig. 1) generally refers to the continental shelf area (<200 m depth) off San Francisco between Pt. Reyes (38.0°N) and Pt. Montara (37.5°N). The area of this study is somewhat larger, extending south to Pt. Año Nuevo (37.1°N) and offshore to the 2000 m isobath. The coastline and bathymetry are generally oriented in a northwest/southeast direction. San Francisco Bay lies inside of the narrow entrance of the Golden Gate. Hook-shaped Pt. Reyes is one of the most

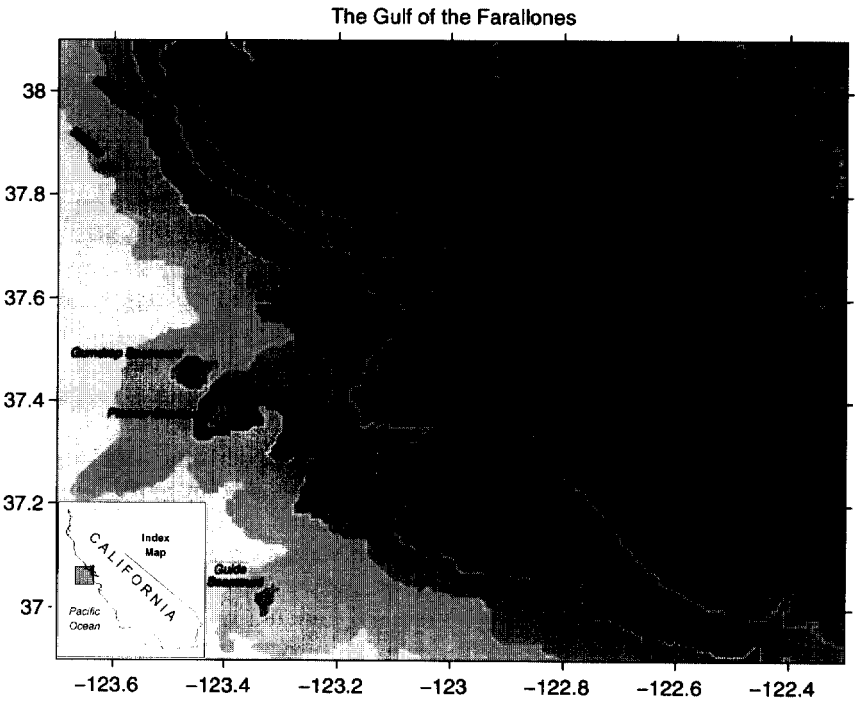

Fig. 1. The Gulf of the Farallones. The study area extends from Point Reyes to Point Año Nuevo and seaward from the coast to about the 2000 m isobath. Bathymetry zones 0–200 m, −1000 m, −2000 m, −3000 m, and >3000 m have gradually decreasing shading. Locations of current meter moorings used in the model are indicated by large open circles.

prominent points along the coast of California, extending seaward about 15 km and somewhat sheltering the inshore portion of the Gulf of the Farallones from the frequent northwesterly winds.

The bathymetry of the region is complex. The continental shelf of California is generally very narrow (in many places 6–8 km), but off the Golden Gate it widens to almost 50 km. Near the shelf break between 37.7°N and Pt. Reyes lie the Farallon Islands and Rittenburg and Cordell Banks. The continental slope varies in steepness, from 1 : 7 between 37.7°N and 38.0°N to 1 : 35 at 37.25°N. The continental slope is broken by several small, narrow canyons in the north and by the relatively large Pioneer Canyon near 37.3°N. A chain of seamounts lies offshore of the 1800 m isobath. Pioneer Seamount, rising to 950 m at 37.35°N, is the most prominent.

Coastal sea level and current meter analyses have shown that the tides off the west coast of North America are predominantly semi-diurnal. Large-scale numerical tidal models (Hendershott, 1973) indicate that the semi-diurnal tides are primarily composed of a barotropic Kelvin wave moving counterclockwise around an amphidrome located in the NE Pacific. Recent tidal models incorporating satellite altimeter data (Cartwright and Ray, 1991; Egbert et al., 1994) and observations from current meters

and bottom pressure meters (Rosenfeld and Beardsley, 1987; Mofjeld et al., 1995) support this view. The pattern of the diurnal tides is similar, with a south-to-north progression up the coast (Mofjeld et al., 1995), possibly coupled with baroclinic continental shelf waves (Noble et al., 1987). In the vicinity of the Gulf, the complicated bathymetry probably causes substantial spatial variation in the tides and may possibly induce other complex internal motions (Petruncio, 1996). This spatial complexity has been found in the Gulf in moored current meter studies (Noble and Gelfenbaum, 1990; Kinoshita et al.,1992). The complicated and seasonally variable density structure of the water (Steger, 1997) may add a baroclinic component to the tides. In addition, there is a strong tidal jet into the Gulf through the Golden Gate (Largier, 1996; Petzrick et al., 1996). The tidal jet is dominated by the M_2 constituent whose amplitude is more than 1 m/s. Although the jet is strongest within the tidal excursion distance from the Gate (approximately 9 km as evident from the boundary of an ebb tidal delta), it will be shown that the influence of the jet extends seaward as far as

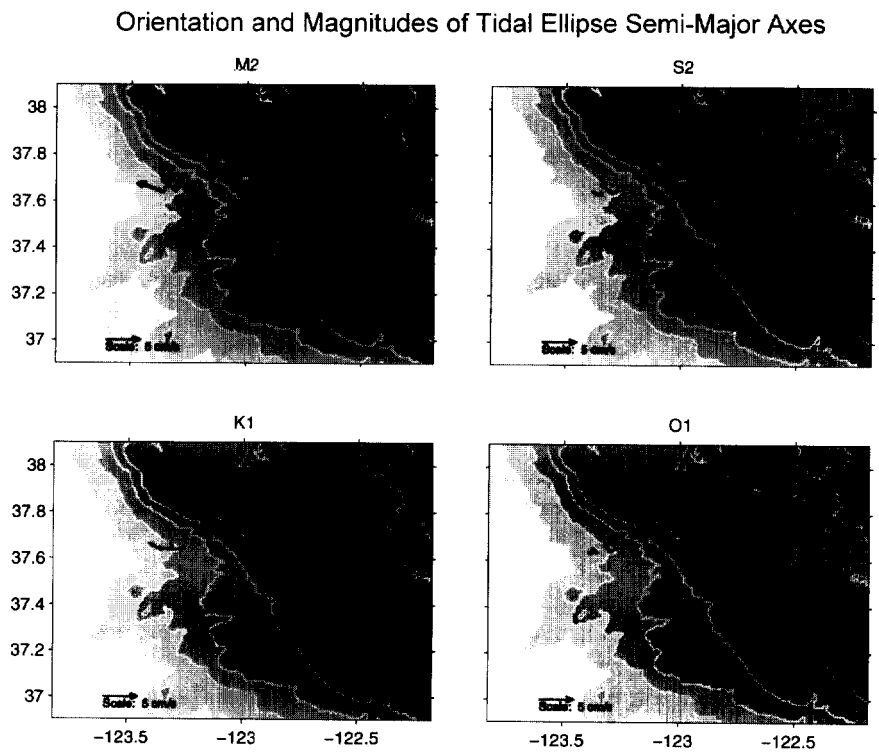

Fig. 2. Orientation and magnitude of the semi-major axes of the M_2, S_2, K_1, and O_1 tidal ellipses calculated for each current meter deployed in the Gulf of the Farallones since 1981. Most moorings had current meters at several depths. Values for each meter are listed in Tables 3–6. Orientation of the semi-major axis means the direction along which tidal current variance is maximized; magnitude means the velocity of the tidal current when aligned with the semi-major axis.

50 km (Section 5). Fluctuations in the temperature and salinity fields associated with this jet can further complicate the density patterns and perhaps increase the complexity of the tidal structure. The orientation and magnitude of the M_2, S_2, K_1, and O_1 semi-major axes calculated from all available current meter moorings in the Gulf are shown in Fig. 2. The offshore tides generally show an alongshore orientation consistent with the notion of alongshore propagating waves. The strongest tides are seen near the Golden Gate, and especially strong M_2 tides are found there. The M_2 tide is influenced by the Golden Gate tidal jet many kilometers seaward. The K_1 tide is apparently amplified over the shelf, as previously noted by Noble and Gelfenbaum (1990). At each tidal frequency, there appears to be considerable variance in the orientation, magnitude, and phases at the different current meters and moorings, even over depth on a single mooring. However, there is no obvious systematic pattern on the moorings to imply a strongly baroclinic tidal structure.

3. Data

ADCP vessel and moored current meter data were combined to form the database for the tidal model. Twenty-seven moorings with 69 instruments deployed in the Gulf of the Farallones since 1975 have been identified (Appendix A). Of these, hourly averaged measurements from 15 moorings (Fig. 1), with a total of 42 instruments, were used in this analysis. The observations were well distributed in time and space (Fig. 3). Data from instruments deployed at depths greater than 500 m were not used in this study so that the current meter and ADCP data sets would be generally comparable. Instruments moored very close to shore are presumably affected by dynamics not of interest to the general tidal circulation in the main part of the Gulf and so were excluded as well. Current meter moorings provide dense coverage at single locations (compare Figs. 1 and 3). The earliest moored observations are from 1981 (the SuperCODE experiment).

ADCP vessel data began in 1991. These data provide good spatial coverage within the region of the model (37.2°N–37.8°N and 123.3°W–122.7°W). Seven cruises with 150 kHz ADCP units provided the spatial data within the geographic boundaries of the Gulf. In general, ADCP ensembles were averaged over 15 min. Velocity measurements were collected in 4 or 8 m depth bins.

ADCP data were collected by the Tiburon Laboratory of the National Marine Fisheries Service aboard the NOAA Ship DAVID STARR JORDAN during springtime surveys of juvenile rockfish in 1993, 1994, and 1995. The surveys and processing of the ADCP data are described in Parker (1996). Each May–June, the survey would run three consecutive south-to-north series of east-west transects from Point Pinos to Bodega Bay, each taking 7–10 days. The three years represent a total of approximately 80 days of ADCP data collected within the Gulf. Because the springtime NMFS Tiburon cruises collected the largest data sets, the years 1993–1995 and the months of May and June have by far the greatest temporal density of observations.

ADCP and current meter data also were collected in 1991 and 1992 during the Slope/Shelf Experiment (SSE). The primary purpose of the year-long SSE, funded by

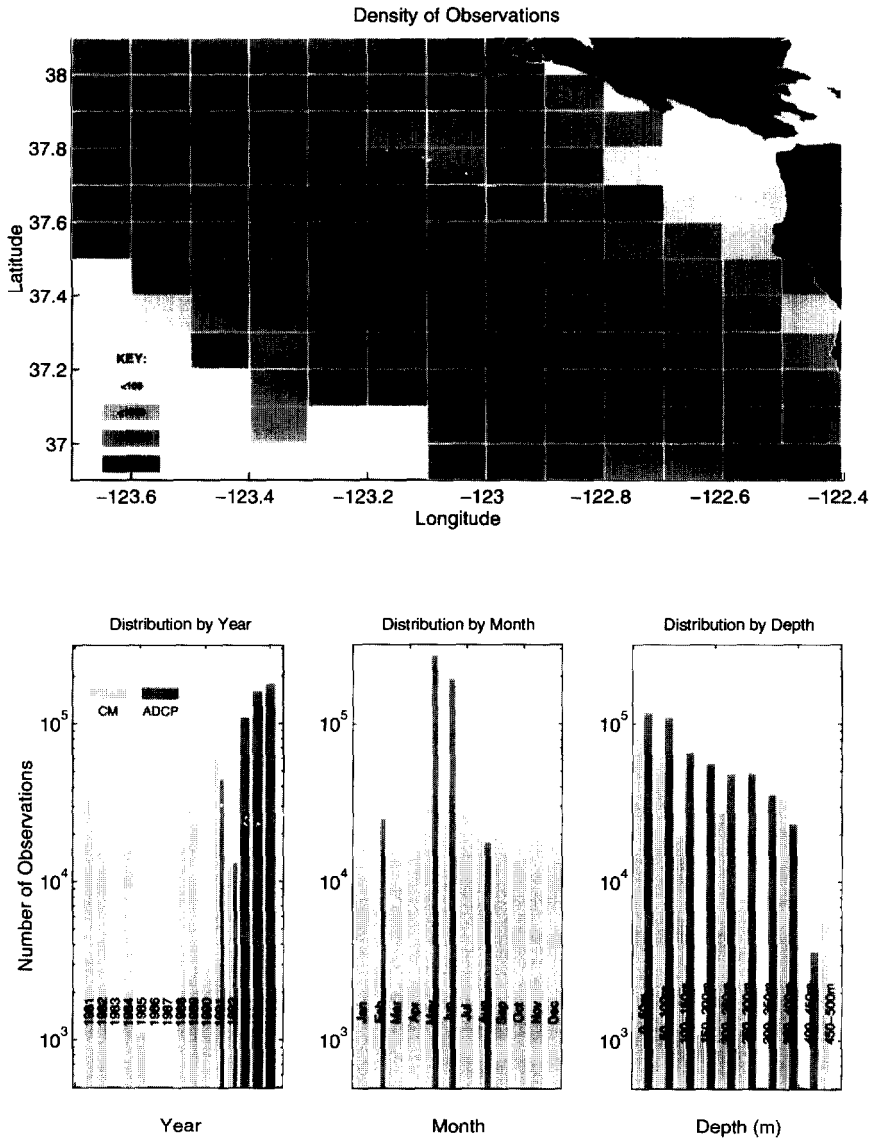

Fig. 3. Distribution of current meter and ADCP observations used to create the tidal model. (a) Spatial distribution. Number of observations in each $1/10^{\circ} \times 1/10^{\circ}$ square is indicated by shading per the legend. The highest density areas correspond to locations of current meter moorings. (b)–(d) Distribution of observations by year, month, and depth. Number of observations are broken into ADCP and current meter (CM) per legend in (b). The y-axes have logarithmic scales. All ADCP data were collected since 1991. The NMFS Tiburon cruises account for the large number of ADCP observations in May–June, 1993–95.

the Environmental Protection Agency and Naval Facilities Engineering Command, Western Division, was to determine the subtidal circulation in the region and how it may affect dredge spoils deposited on the shelf and slope. The study included five ADCP and CTD cruises (February, May, August, and October 1991; and February 1992) of 6–7 days length. Six current meter moorings were deployed from February 1991 thru February 1992, spanning the cruise dates (SSE-A to F in Fig. 1). The collection and processing of the ADCP data are described by Jessen et al. (1992a–d) and Rago et al. (1992). The October 1991 ADCP data are not used because they were not processed correctly until after the tidal model was run. Kinoshita et al. (1992) describe the collection and processing of the current meter data. Data from 22 instruments deployed during this study were included in the model.

The US Geological Survey and U.S. Army Corps of Engineers sponsored a series of moorings in 1989 and 1990 to study sediment transport patterns in the Gulf. The hourly data from these moorings (346, 334, 335, 1M, and B1B in Fig. 1), which total 12 instruments, were included in the study. Mooring 346 was deployed for $1\frac{1}{2}$ months; 334, 335, and 1M for five months; and B1B for thirteen months. The moorings are described in detail in Noble and Gelfenbaum (1990) and Sherwood et al. (1989).

Two current meter moorings containing two instruments each (CCCCS-K and -L in Fig. 1) were deployed in the Gulf of the Farallones for twelve months in 1984 as part of the Central California Coastal Circulation Study (CCCCS), a study of the slope and shelf currents between Pt. Conception and San Francisco Bay (Bratkovich et al., 1991; Chelton et al., 1987; Chelton et al., 1988). Two moorings (H3 and H4 in Fig. 1) were also deployed in the Gulf in 1981 and 1982 as part of SuperCODE (Coastal Ocean Dynamics Experiment) (Denbo et al., 1984; Strub et al., 1987). H4, the deeper mooring, was repeatedly hit by fishermen so that the records from its three meters are fairly short and broken. The entire record (fifteen months) from the single meter on H3 was used in the tidal model.

4. Building the empirical tidal model

This tidal model extends the tidal analysis methods of Foreman (1978), where the observed velocity is decomposed into a mean steady current and tidal currents that vary in time at a finite number (n) of frequencies. An amplitude and phase for each tidal frequency are estimated by expressing the linear current meter record in the form:

$$\begin{aligned} u(t) &= u_0 + \sum_{k=1}^{n} a_k \cos(2\pi\omega_k t) + b_k \sin(2\pi\omega_k t), \\ v(t) &= v_0 + \sum_{k=1}^{n} c_k \cos(2\pi\omega_k t) + d_k \sin(2\pi\omega_k t), \end{aligned} \tag{1}$$

where ω_k is the tidal frequency for the kth constituent and u and v are the observed total velocity components at each time t. The coefficients a_k, b_k, c_k, and d_k are solved for using the method of least squares, which subsequently can be used to predict u and

v for any time t. Candela et al. (1990, 1992) incorporated spatial variation into the method:

$$\begin{aligned} u(\lambda, \phi, t) &= u_0(\lambda, \phi) + \sum_{k=1}^{n} [(a_k + b_k\lambda + c_k\phi)\cos(2\pi\omega_k t) \\ &\quad + (d_k + e_k\lambda + f_k\phi)\sin(2\pi\omega_k t)], \\ v(\lambda, \phi, t) &= v_0(\lambda, \phi) + \sum_{k=1}^{n} [(g_k + h_k\lambda + i_k\phi)\cos(2\pi\omega_k t) \\ &\quad + (j_k + k_k\lambda + l_k\phi)\sin(2\pi\omega_k t)], \end{aligned} \tag{2}$$

where λ and ϕ are longitude and latitude.

Candela et al. vertically integrated the ADCP observations for input to their model. However, current meter observations in the Gulf of the Farallones show marked variations in tidal amplitude and phase at different depths on the same mooring (Fig. 2, Tables 3–6 in the Appendix). We therefore included depth (z) in the spatially varying model:

$$\begin{aligned} u(\lambda, \phi, z, t) &= u_0(\lambda, \phi, z) + \sum_{k=1}^{n} [(a_k + b_k\lambda + c_k\phi + d_k z)\cos(2\pi\omega_k t) \\ &\quad + (e_k + f_k\lambda + g_k\phi + h_k z)\sin(2\pi\omega_k t)], \\ v(\lambda, \phi, z, t) &= v_0(\lambda, \phi, z) + \sum_{k=1}^{n} [(i_k + j_k\lambda + k_k\phi + l_k z)\cos(2\pi\omega_k t) \\ &\quad + (m_k + n_k\lambda + o_k\phi + p_k z)\sin(2\pi\omega_k t)]. \end{aligned} \tag{3}$$

Coefficients for the mean current and each tidal frequency are combined into a single matrix and fitted simultaneously to the observed velocities using the method of least squares.

The form of the coefficients, either polynomial form or transcendental forms such as the multi-dimensional biharmonic Green's function (Candela et al., 1990, 1992), can be chosen to best interpolate across the model region. This is not known a priori. To test the sensitivity of this tidal model to the order of the polynomial, Steiner (1994) ran a number of test cases using synthetic transport data sets comprised of a mean flow and an M_2 and K_1 tide whose spatial structure was known. These were then modeled with different orders of polynomial fits. In each case, the total flow was correctly modeled but the partitioning of the flow components (mean flow, M_2, K_1) varied radically depending on the polynomial order.

To illustrate this, the case is shown for a synthetic current data set representative of ADCP data that would be collected from a ship during a four day cruise. The synthetic currents are the sum of a steady flow that increases from -0.1 to 0.1 m/s linearly with distance from shore, an M_2 component with a spatially constant amplitude of 0.04 m/s, and a third-order K_1 constituent that decreases from 0.06 to 0.03 m/s with distance offshore. The model domain is a box with a step in bathymetry representing the continental margin.

When the synthetic data is fit using a third-order polynomial for the mean flow, a linear polynomial for the M_2 component, and a second-order polynomial for the K_1 component, the individual flow components are poorly modeled even though the correlation between the synthetic "observed" and modeled flow was perfect (Fig. 4). The model misallocates the energy between the mean and tidal components and, in this case, even portrays alongshore variability even though the synthetic data varied only in the cross-shore direction. In general, Steiner found, higher-orders of fit can cause serious misrepresentations of the tidal flows due to overfitting of the spatial structure and incorrect energy allocation.

Steiner (1994) concluded that, unless the tidal structure is already well understood, it is best to use a low-order polynomial fit for all tidal constituents. Another advantage of lower-order polynomial coefficients is that, as noted by Candela et al. (1990, 1992), the model is better behaved near the boundaries of the data coverage. This is especially important if the model is used to extrapolate tides outside the region of data coverage or through pockets of low data density. Allen (1995) also experimented

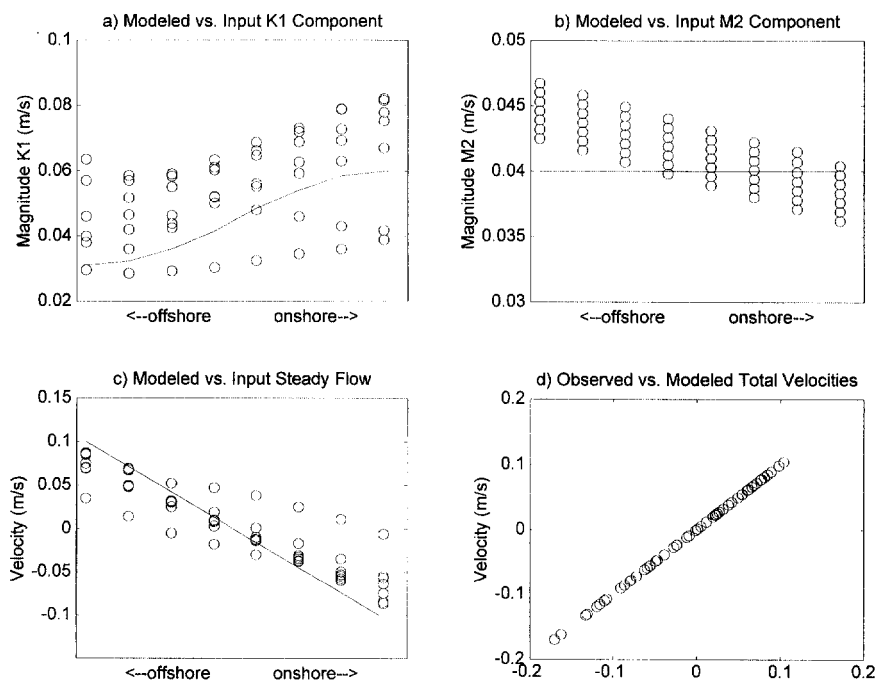

Fig. 4. Modeled versus synthetic amplitudes for (a) K_1 tidal constituent, (b) M_2 constituent, and (c) steady (non-tidal) current. Scaled distance from coast shown on x-axis. Synthetic values, which vary only in the cross-shore direction, are shown by solid lines. Open circles denote modeled values at eight locations on seven cross-shore sections. Distribution of circles in each panel represents alongshore variability of model results. (d) Correlation between synthetic and modeled total current throughout model domain, showing perfect correlation.

using linear vs. second-order polynomials to detide ADCP data in the Iceland–Færœs Strait and concluded that arbitrarily increasing the order did not significantly improve the tidal fit. For these reasons we have chosen linear coefficients $(a_k + b_k\lambda + c_k\phi + d_k z)$.

Computing the coefficients of the linear 3-D tidal model and using them to predict tides or determine tidal ellipse characteristics is straightforward and presented in Appendix B.

5. Results

The tidal model was run with several combinations of current data sets (Figs. 5–10). Tidal ellipses were estimated for the M_2, S_2, K_1 and O_1 constituents for all available data (Case 1), data from all the current meters (Case 2), ADCP data from the NMFS Tiburon surveys (Case 3), ADCP data from the May 1991 SSE cruise (Case 4), ADCP data from four SSE cruises (Case 5), and data from the NMFS Tiburon surveys divided into northern and southern fields (Case 6). Table 1 summarizes the model runs and the size and seasonality of the input data sets. The results varied, sometimes dramatically, depending on the quantity, type, seasonality, and coverage of the input data.

Case 1: When all available current meter and ADCP data are used to create the tidal model (Fig. 5), the constituent fields show the characteristics expected from the tides calculated from current meter series.

The M_2 tide is generally oriented with the northwest-southeast large-scale coastline except near the Golden Gate, where its orientation adjusts to tidal flow through the Gate. Maximum velocities are fairly consistent, ranging from 3 to 5 cm/s. The highest velocities are on the shelf near the Gate. Tidal ellipses are mostly rectilinear. The S_2 tide also follows the large-scale coastline but does not appear to be affected by the tidal jet through the Gate. Maximum velocities vary considerably. Velocities approach 3 cm/s in deep water and near the Gate, but diminish near the shelf break. There appears to be a point near 37.5°N, 123.0°W where the tidal velocities are near zero. The tidal ellipses are mostly rectilinear but the ellipses become more circular as velocities decrease, especially in the northern part of the Gulf.

The K_1 tide follows the bathymetry throughout most of the Gulf, but near the Gate it is oriented perpendicular to the bathymetry. Since it is not seen in either the Tiburon- or current meter-only models (Cases 2 and 3), this may be a model artifact. Maximum velocities are in the 2–4 cm/s range, with the highest velocities on the shelf and the lowest velocities near the shelf break. Tidal ellipses are nearly circular in the southeast corner but mostly rectilinear elsewhere. The O_1 tidal field looks similar to that of the K_1 but with lower maximum velocities, in the 1–3 cm/s range.

In the mean flow, poleward flow is seen offshore of the shelf break. Highest velocities are in the southwest corner, over 5 cm/s. Equatorward flow, mostly in the 1–3 cm/s range, is seen on the shelf.

Cases 2 and 3: When using all the current meter data (Case 2, Fig. 6) or all of the ADCP data from the Tiburon cruises (Case 3, Fig. 7), the tidal fields are comparable

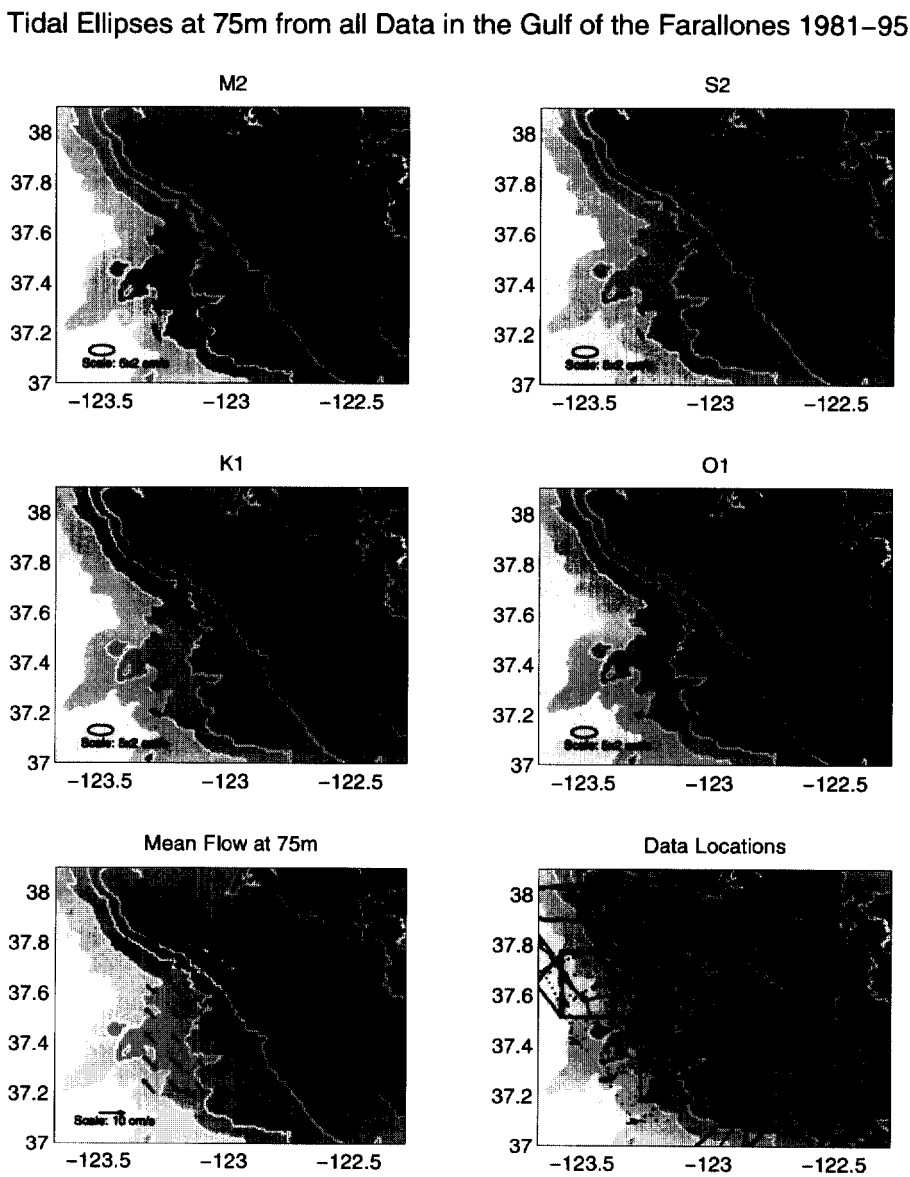

Fig. 5. Model results using all available ADCP and current meter observations. Model tidal ellipses at 75 m depth on a $1/10^{\circ} \times 1/10^{\circ}$ grid between 37.2°N–37.8°N and between 123.3°W–122.8°W are plotted for the (a) M_2, (b) S_2, (c) K_1, and (d) O_1 tidal frequencies. Scale ellipses with a 5 cm/s semi-major axis and 2 cm/s semi-minor axis are shown. (e) Model mean flow at 75 m depth. Scale vector of 10 cm/s is shown. (f) Locations of data observations. Locations of ADCP ensembles are shown as a dots. Locations of current meter moorings are indicated by larger open circles.

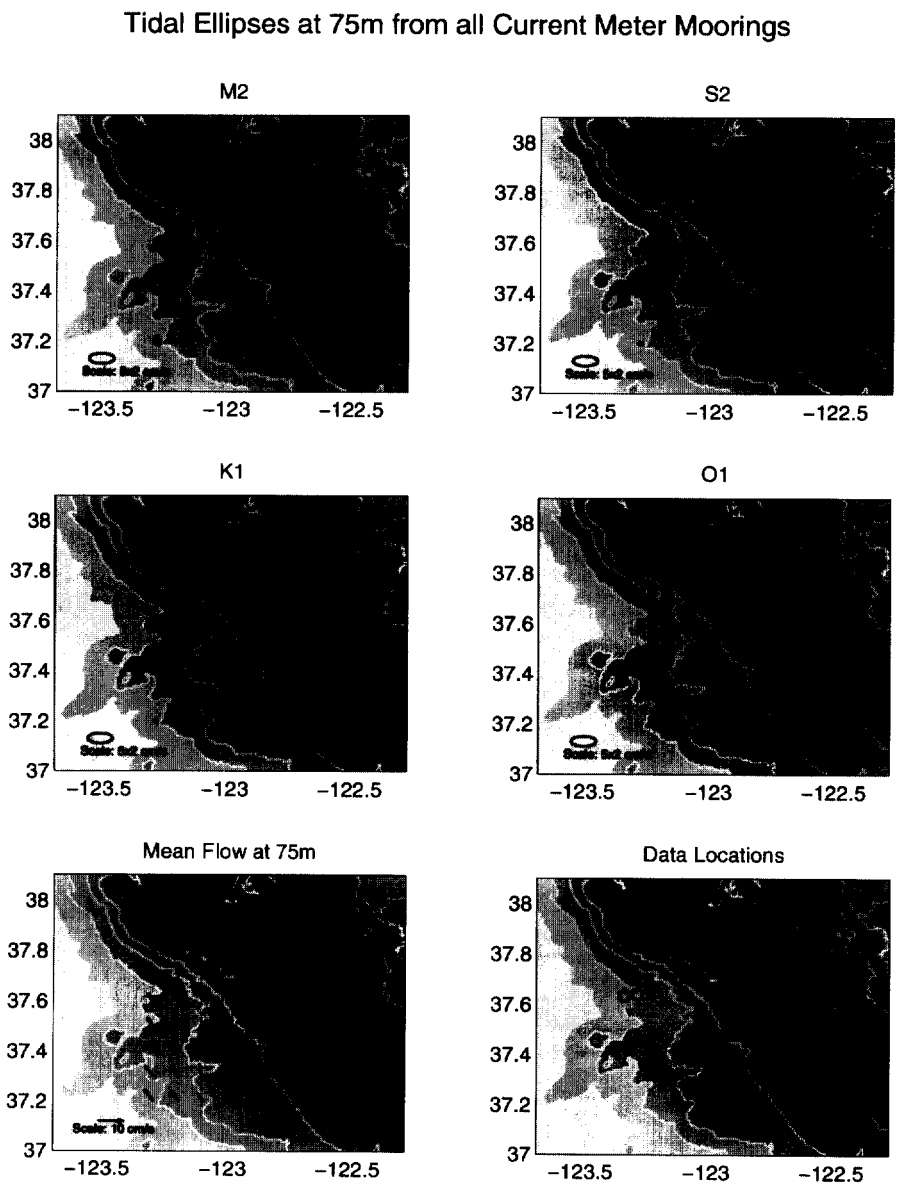

Fig. 6. Model results using all available current meter observations. Otherwise, same as Fig. 5.

to those estimated from the complete data set. Velocity amplitudes fall in the 1–6 cm/s range and orientations of the tidal ellipses, especially offshore, more or less follow the large-scale coastline. Results from these two cases look comparable even though they are created using independent data, suggesting a consistent solution is not dependant on the source (ADCP or current meters) of the velocity observations. There are some

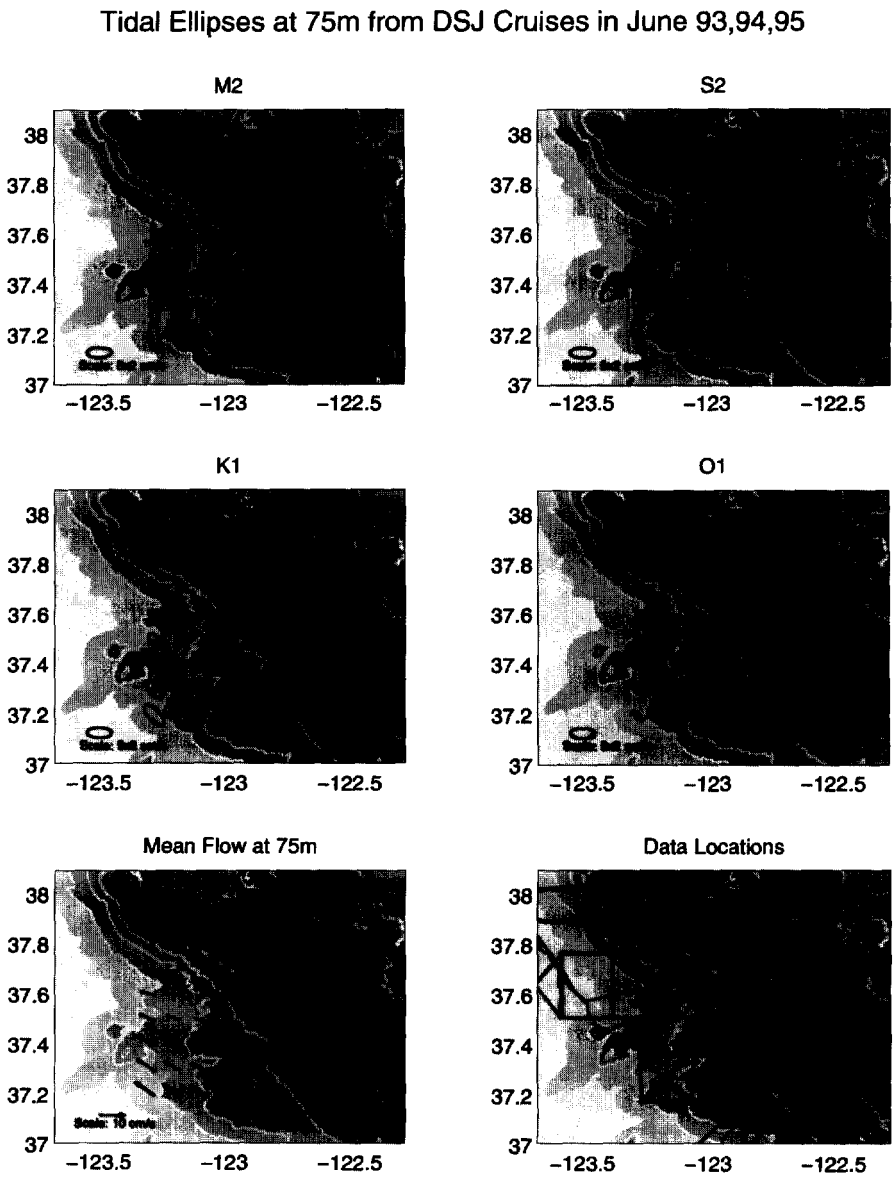

Fig. 7. Model results using all available ADCP observations from the NMFS Tiburon cruises in May–June, 1993–95. Otherwise, same as Fig. 5.

differences between Figs. 5–7 in the size of the semi-minor axes and small differences in tidal velocities and orientation, especially in the corners of the model domain where the data observations were sparse. But on the whole the tidal fields are comparable and the similarity in the mean flow fields is striking.

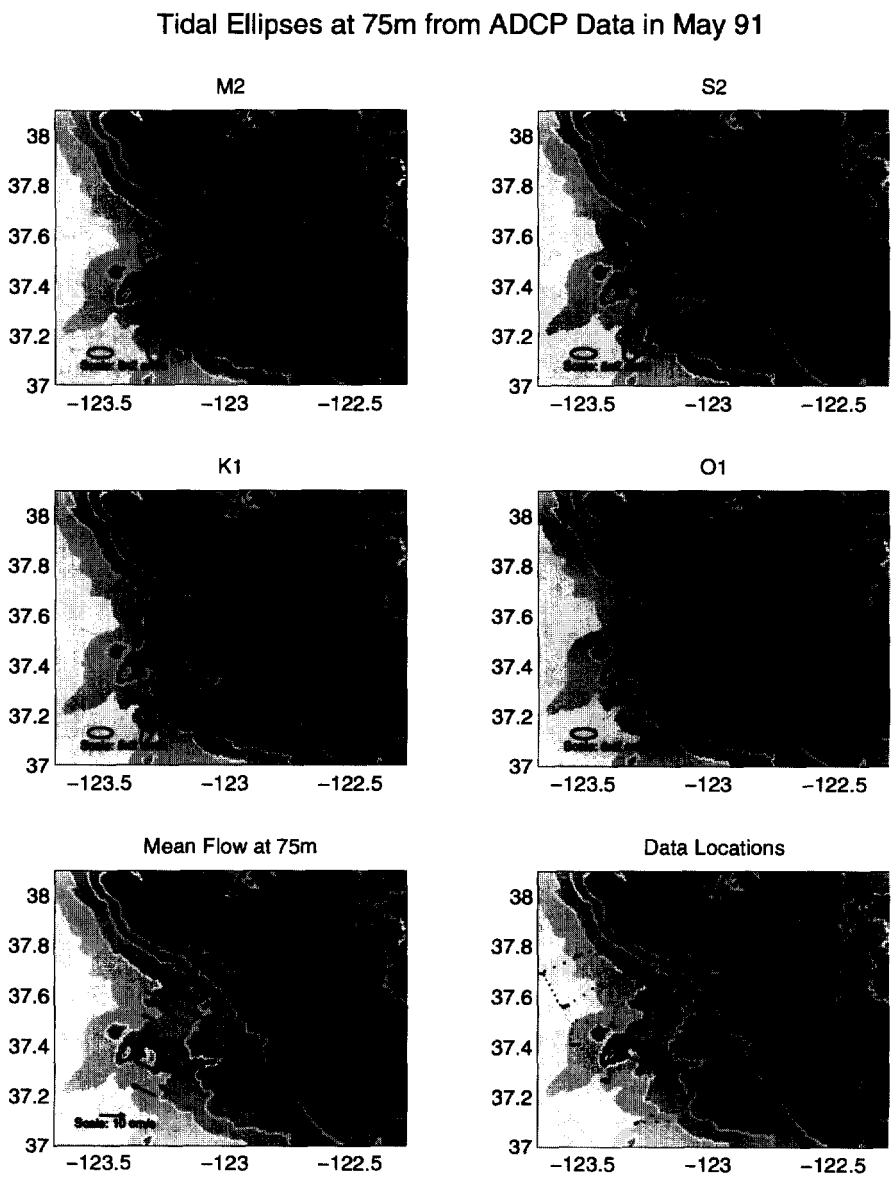

Fig. 8. Model results using ADCP observations from May 1991 cruise of the Slope/Shelf Experiment (SSE). Otherwise, same as Fig. 5.

An interesting feature of the model run with the current meter data alone (Fig. 6) is the apparent amplification of tides over the shelf. This effect was previously noted in the diurnal tides by Noble and Gelfenbaum (1990). Amplification of this sort also has been seen over the Yermak Plateau (Prazuck, 1991). A somewhat different picture is

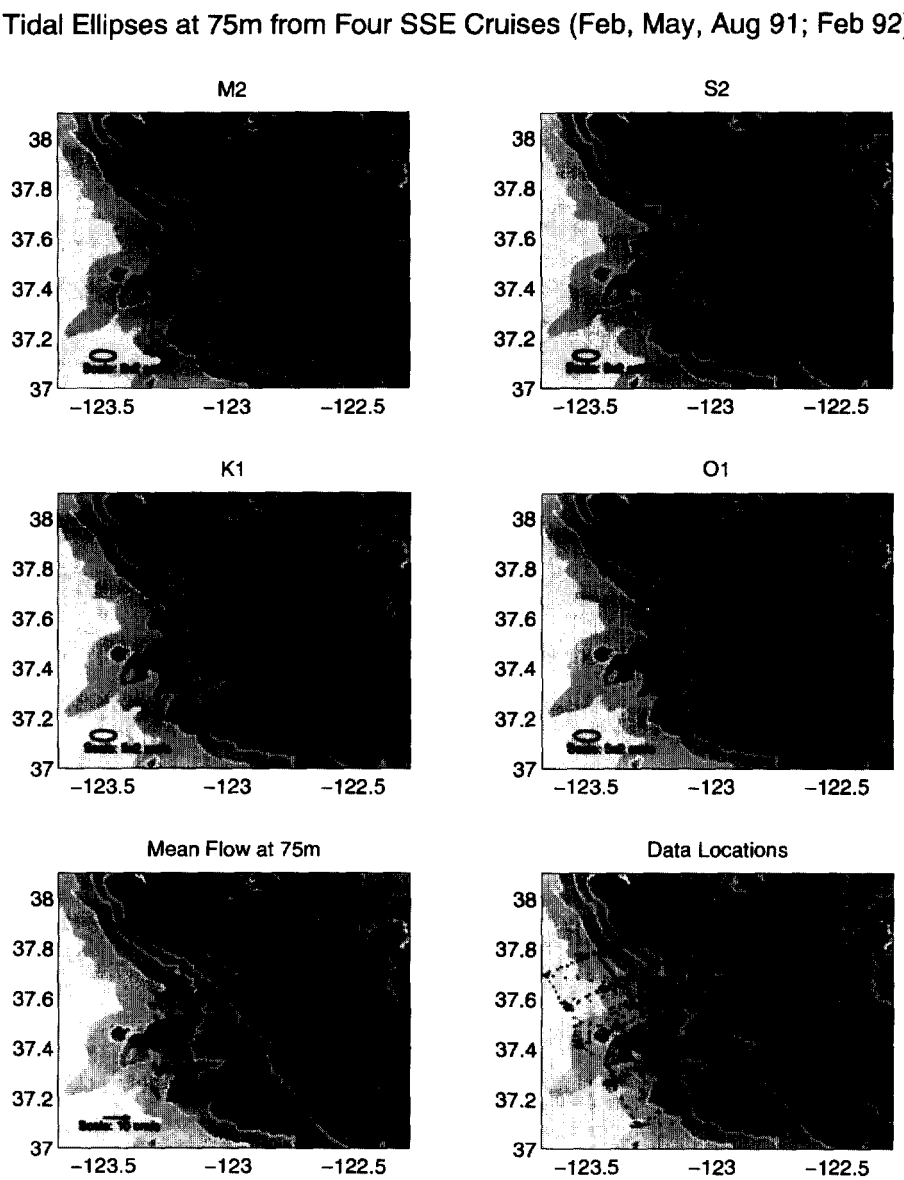

Fig. 9. Model results using ADCP observations from the February, May, and August 1991 and February 1992 cruises of the Slope/Shelf Experiment (SSE). Otherwise, same as Fig. 5.

seen in the Tiburon ADCP data model fields (Fig. 7). Instead of amplification over the shelf, there appears to be a minimum along the shelf break, especially in the K_1 and S_2. From the data in hand, it is impossible to say whether the minimum is real (perhaps a seasonal effect since the Tiburon data were collected exclusively in

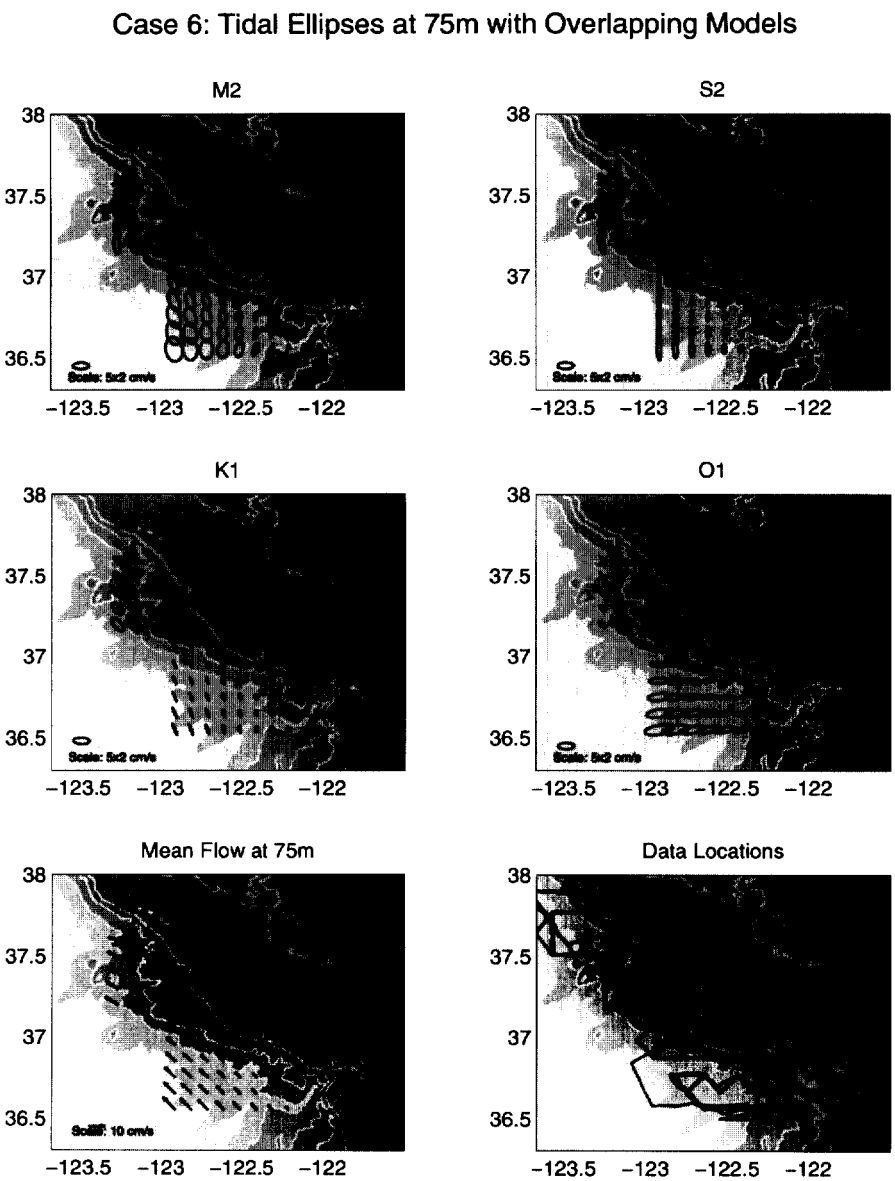

Fig. 10. Results from two tidal models: one using ADCP data from the northern legs of the NMFS Tiburon cruises and another using data from the southern legs. Model tidal ellipses at 75 m depth for the northern model are shown for a 1/10° × 1/10° grid between 37.2°N–37.8°N and between 123.3°W–122.8°W; for the southern model ellipses are shown for a 1/10° × 1/10° grid between 36.55°N–37.35°N and between 122.95°W–122.05°W. (f) Locations of ADCP ensembles for the northern model are indicated by small black dots and locations of the ensembles for the southern model are indicated using small circles. Otherwise, same as Fig. 5.

Table 1
Characteristics of data used in model runs. Six models of the tides in the Gulf were created, each using different empirical data sets, to show the dependence of the model on the type and quantity of input observations

Case	Figure	Data used to create the tidal model	Number of observations	Seasonality
1	5	All available ADCP and current meter data	704,780	All seasons
2	6	All available current meter data	254,651	All seasons
3	7	ADCP data from the three Tiburon Rockfish survey cruises	455,090	May–June
4	8	ADCP data from the May 1991 SSE cruise	14,554	May
5	9	ADCP data from four SSE cruises	58,359	Feb/May/Aug
6	10	ADCP data from the three Tiburon Rockfish survey cruises divided into northern and southern fields	455,090 (north) 435,512 (south)	May–June

May/June) or an artifact of the model (perhaps caused by the linear form of the model, a few noisy data points, a relative dearth of ADCP data in the southwest corner of the field, or other problems). However, the shelf break minimum also is seen in the model run with data south of the Farallones region (Case 6, Fig. 10). To test if the linear polynomial fit causes the "saddle" shape at the shelf break, the Tiburon data were split into two distinct data sets, one over the shelf and one over the slope and deep water. There was a slight (1/10° latitude) overlap in the data sets. Each nearly independent set produced model fields that had velocities that gradually diminished towards the shelf break. This convinced us the choice of polynomials was not the cause of the minimum at the shelf break.

The mean flow fields in the Tiburon and current meter tidal models show similar features to the mean flows in Case 1. Poleward flow, stronger in the springtime Tiburon fields, is seen offshore over the slope. Weaker, equatorward currents are prevalent over the shelf.

Case 4: To test the effectiveness of using ADCP data from a single cruise to characterize the regional tidal fields, the model was run using only data from the May 1991 SSE cruise (Fig. 8). Model tidal amplitudes are far too high, and the tidal fields exhibit areas of extreme convergence and divergence. Ellipse orientations differ wildly from ellipses calculated from current meters (Tables 2–5, Fig. 2) or from the model using all available data (Fig. 5). During the SSE cruises, the ship crossed the strongly sheared alongshelf current twice a day, or roughly at the same frequency as the semi-diurnal tidal constituents. Considering the relatively short duration of the cruise, this may bias the model results. Models created using the other individual SSE cruises (not shown) had similar unreasonable characteristics. *In areas of complex tidal patterns or relatively weak tides and strong subtidal currents, data from a single short cruise are insufficient to create realistic empirical tidal estimates.*

Case 5: Increasing the data set to four ADCP cruises (Fig. 9) helps dramatically, but tidal velocities are still too high in some areas and the orientations often appear

unrealistic compared to that expected from current meter observations. For example, the M_2 rotation near the Gate is absent, and anomalously strong K_1 currents are seen in the northeast corner of the region. This four-cruise model could be applied to detide the SSE data set, and the overall tidal variance would be reduced, but probably at a cost of inducing abnormal velocities in some areas. The mean flow field features a reasonable poleward flow over the slope and weak and variable currents over the shelf. The mean flow using only the May 1991 cruise data (Fig. 8) shows greater poleward (equatorward) flow over the slope (shelf) than the total solution, which spans all seasons. The seasonal intensification of the countercurrent over the slope in the spring agrees with the findings of Collins et al. (1996) who examined $5\frac{1}{2}$ yr (May 1989–February 1995) of current meter data collected off Point Sur ($\sim$170 km south of the Farallones) and found an annual signal in alongshore velocity that peaks in June and is weakest in October. The equatorward shelf currents, however, are probably a response to increased equatorward winds. Alongshore surface stress off central California is highest in April–June (Nelson, 1977; Schwing et al., 1996).

Case 6: To see how models of two regions would overlap, the model was run with data from the region south of the Gulf (off Monterey Bay). This southern region slightly overlapped the Gulf region (Fig. 10). Where the models overlap, velocities and orientations are similar, again giving assurance that with sufficient data the model captures the essential characteristics of the tidal fields.

6. Model accuracy and sensitivity

From our analysis of the tidal model results using different input data sets, two immediate conclusions are drawn. First, the greater the number of observations used to create the model, the more the tides resemble what we expect to see from tidal analyses of the current meters and our understanding of the tides as poleward propagating Kelvin waves along the eastern boundary of the North Pacific. Secondly, models created with completely independent (but large) data sets produce tidal constituent fields that show similar structures and patterns.

In general, when larger data sets are input, the model reproduces most of the features of the expected mean and tidal fields. The tides mostly follow bathymetry. The diurnal tides are amplified over the shelf. The influence of tidal flow through the Golden Gate is suggested by the orientation of the M_2 ellipses. Tidal velocity amplitudes are in the ranges seen by fixed current meters (as listed in the tables in Appendix A). Mean poleward flow offshore and equatorward flow on the shelf is indicated. The model is not sophisticated enough, however, for us to say with confidence that other features, such as the velocity minimum near the shelf break, are real.

The empirical method is capable of solving for any tidal constituent (assuming the Rayleigh criterion is met, as discussed below). However, since our main purpose was to reduce tidal frequency energy we only used the model to determine the four constituents with the highest amplitudes as determined from current meter analyses (Noble and Gelfenbaum, 1990). Current meter records also show considerable

energy at other frequencies, especially the $P_1(P_1/K_1 \approx 0.4)$, $N_2(N_2/M_2 \approx 0.25)$, and $K_2(K_2/M_2 \approx 0.25)$. Some of the features we see in the data-sparse model runs, where the Rayleigh criterion is not met, may be artifacts caused by "beating" between adjacent analyzed and non-analyzed frequencies. We also do not include nodal modulation in the model to account for the 19-yr cycle in tidal amplitude. Over the period of the observations in the Gulf, the K_1 nodal correction factor varies by $\sim 20\%$ and the M_2 nodal correction value varies by $\sim 7\%$.

Spectral analysis of the current meter records also shows considerable energy at the local inertial frequency (19.6 h). In addition, the tidal jet and interactions of the current with the steep continental slope may be constant sources of inertial energy. Internal tides and inertial motions are not addressed in the model since they are usually intermittent. It is also assumed that the tides are stationary on seasonal and longer time scales. Tidal analyses on 16-day segments from several current meters supported this assumption.

The size of the input data set needed to resolve the currents adequately is probably a function of the complexity of the mean and tidal circulations in a region, as well as their relative magnitude. To estimate the statistical accuracy of our tidal models using the various input data sets (Table 1), a variant of the bootstrap method (Kinsella, 1986) is applied. The bootstrap method measures the sensitivity of the empirical method to the distribution and quantity of input data. It is also a measure of how reliable (consistent) the model parameters are in determining the distribution of energy between the steady flow and the tidal frequencies. In many ways it is preferable to examining the conditioning of the least squares matrix, which only explains how well the numerical solution fits the total flow. Steiner (1994) has shown that the fit to the total flow is not representative of the performance of the model parameters.

The bootstrap is run as follows: a sample set of n observations is built from the original n-length data set by randomly selecting an observation and "replacing it" before making the next random selection. Because of replacement, the sample set may have duplicates of or lack some observations from the original set. The model is run using the sample set and model output values recorded. This was repeated 128 times, after which histograms of the model output values were normally distributed and statistical properties could be derived. Standard errors were calculated for the 75 m output values in a $1/10^\circ \times 1/10^\circ$ grid and contoured (Fig. 11). The standard errors of

Fig. 11. Contours of standard errors of the mean flow and M_2 and K_1 tidal ellipse parameters for the tidal models created with (a) (left column) only ADCP data from the May 1991 Slope/Shelf Experiment cruise, (b) (2nd column) ADCP from four Slope/Shelf experiment cruises, (c) (3rd column) ADCP data from the three NMFS Tiburon cruises, (d) (4th column) all available current meter data, and (e) (right column) all available ADCP and current meter data. Standard errors were calculated using the bootstrap method for locations on a $1/10^\circ \times 1/10^\circ$ grid throughout the model region. Down each column are (i) (top) contours of standard error of the mean flow, (ii) contours of standard error of the semi-major axis of the M_2 tidal ellipse with background shading where darker shades indicate regions of smaller standard errors of the M_2 semi-minor ellipse, (iii) contours of standard error of the orientation of the M_2 tide with background shading indicating regions where the tidal ellipse is less (lighter shades) or more (darker shades) eccentric, (iv) contours of standard error of the phase of the M_2 tide with background shading also indicating less (lighter shade) or more (darker shade) tidal ellipse eccentricity, (v)–(vii) same as subfigures (ii)–(iv) except calculated for the K_1 tidal constituent.

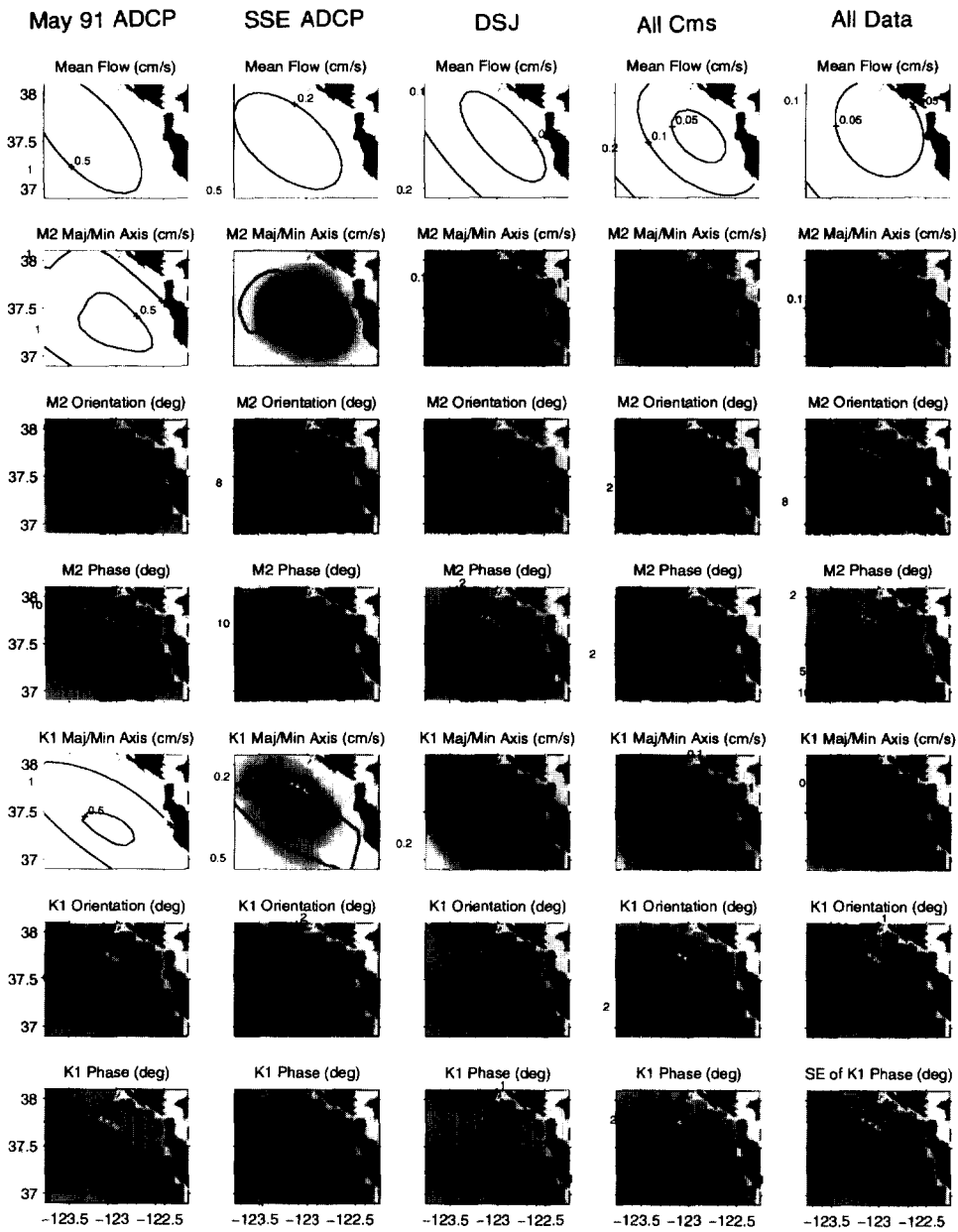
Standard Errors of Model for Various Input Data Sets
May 91 ADCP
SSE ADCP
DSJ
All Cms
All Data
Mean Flow (cm/s)
M2 Maj/Min Axis (cm/s)
M2 Orientation (deg)
M2 Phase (deg)
K1 Maj/Min Axis (cm/s)
K1 Orientation (deg)
K1 Phase (deg)
SE of K1 Phase (deg)
38
37.5
37
-123.5 -123 -122.5

the mean flow and ellipse characteristics of the M_2 and K_1 tides are shown for the models using only the ADCP observations from the May 1991 SSE cruise (Case 4), all ADCP data from four SSE cruises (Case 5), ADCP data from the Tiburon cruises (Case 3), all current meter observation (Case 2), and all observations (Case 1). The S_2 and O_1 model errors (not shown) are similar to the M_2 and K_1, respectively.

Areas of high error in the orientation and phase are associated with regions of almost circular tidal ellipses (Figs. 5–9). Because small changes in the length of the axes of nearly circular ellipses can produce large changes in phase and orientation, statistics in these cases become ambiguous. For large data sets, generally, standard errors are less than 0.2 cm/s and 2° for tidal amplitude and phase, respectively, and less than 0.1 cm/s for mean flow.

The larger the input data set, the smaller the standard errors of the model outputs (Fig. 12). For example, at the center of our model domain (123°W, 37.5°N) the standard error for the M_2 amplitude drops from 0.4 cm/s for our May 91-only model (14,554 observations) to less than 0.03 cm/s for a model using all the data (704,780 observations) (Fig. 11). The standard errors drop by an order of magnitude as the number of input data increases from 14,000 to 200,000 observations, after which additional observations add little to the statistical accuracy. The bootstrap method

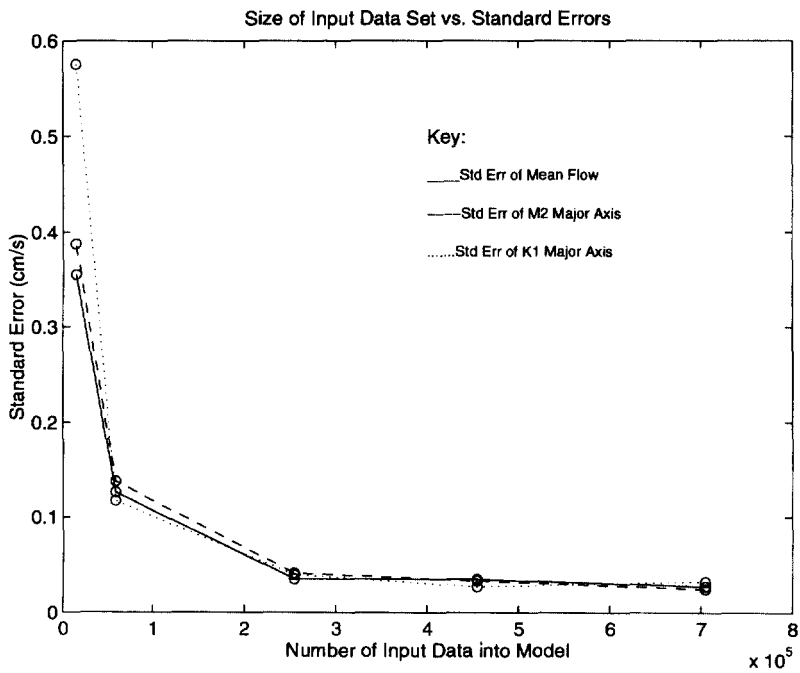

Fig. 12. Relationship between the number of observations input into the tidal model and the standard errors of the mean flow and the semi-major axes of the tidal ellipses of the M_2 and K_1 tides.

thus provides a means of estimating how many observations are necessary in a region to produce a reasonable model. For O(200,000) observations, the standard errors of the model are small, less than 0.05 cm/s ($\pm 2\%$) for both the mean flow and the tidal ellipse axes.

Models run with smaller-sized data sets are subject to problems meeting the Rayleigh criterion. Godin (1972) points out that to resolve two tidal frequencies, the length of observations must exceed one cycle of the difference between the frequencies, i.e. $n\Delta t \geqslant |\omega_1 - \omega_2|^{-1}$ where $n\Delta t$ is the measuring period. This is inadequate for spatial tidal analysis, so we define a multi-dimensional Rayleigh criterion:

$$n\Delta t d^{-1} \geqslant |\omega_1 - \omega_2|^{-1} \tag{4}$$

where d is the number of dimensions in the model. Since our model uses linear coefficients $(c_1 + c_2\lambda + c_3\phi + c_4 z)$, $d = 4$. The multi-dimensional criterion provides a lower bound to the number of observations, since an even spatial and temporal distribution of the data is assumed. In other words, the independence of the observations is important. For example, an ADCP record consisting of an ensemble of many velocity observations at depth intervals beneath the ship can only be used to resolve linear tides in two dimensions (t and z), and so should be counted as only two observations in meeting the criterion. Thus, the $\sim$500,000 unique observations in t, λ, ϕ, and z with the ADCP count as $\sim$30,000 observations (using 30 as the average number of depths per ensemble). Also, 15-min averaged ADCP data were used. With this number, our model meets the criterion for [(15,000 ADCP records) (2 obs/record) $(\frac{1}{4}$ h)$(4)^{-1}$ + (200,000 current meter obs)(1 hr) $(4)^{-1}]^{-1} = 2 \times 10^{-5}$ h^{-1}, which is sufficient to resolve all standard tidal frequencies. In general, a $d = 3$ model would need 39 hourly ADCP records to discriminate between the diurnal K_1 and semi-diurnal M_2, and 532 hourly ADCP records to discriminate between the M_2 and S_2 tides. For $d = 4$, 52 and 709 h would be needed, respectively.

In the Case 1 (using all available data) baroclinic model, the M_2, S_2, K_1, and O_1 tides account for 10.3% of the variance in u (east–west flow) and 17.8% of the variance in v (north–south flow), less than the tidal variance typically found in current meter records in the Gulf, 29–50% in u and 45–58% in v (Noble and Gelfenbaum, 1990). That the model tides explain less variance is partly accounted for by spatial variation in the non-tidal currents. We also expect that, because of the spatial linearity of the model and its incorporation of many separately collected data sets over a large region, it cannot separate the tides as well as conventional analysis techniques performed on a stationary data set. A major dilemma of the empirical method is that more variance could be explained using higher-order polynomial structure functions, but that in doing so confidence is lost that the model is correctly partitioning the variance between frequencies.

We expected from the historical current meter analyses that the tidal model would find significant variation with depth. In fact the model output, especially when large data sets are used as input, shows very little variation with depth. When the model is run using all available data but without a z (depth) dependence, the tidal fields are nearly identical and almost the same amount of tidal variance is accounted for: 10.1% in u and 17.6% in v. It turns out that fitting many seasons and years of observations

into linear time, latitude, longitude, and depth functions averages out any depth variations in what is seasonally a barotropic system. Tidal ellipses estimated from the model for 75 m depth (Figs. 5–10) are in some places plotted where the depth of water is too shallow for this to be realistic, but as the model varies little with depth and does not incorporate near-bottom friction, the results can be interpreted to represent a mid-layer depth.

Further improvements on the method used here are possible. The creation of the model is currently unconstrained except by the observational data. The model would presumably be improved if some dynamical constraints, such as bathymetry, were incorporated. If the phase and amplitude differences between the tidal currents and sea level were known (or could be inferred from the model results), it may be possible to include additional sea level and bottom pressure observations into the model. This would be a useful addition since in most areas sea level observations are more plentiful and easier to obtain than current observations.

7. Conclusion

This work initially addressed whether, in an area such as the Gulf of the Farallones with complex tidal currents, large mean currents, and probably large internal tides and inertial oscillations, the tidal energy can be reasonably removed from ADCP and current meter observations using the technique of Candela et al. (1990, 1992). We have shown that, with enough data, 4-D velocity data can be "detided" and that, in addition, a model that reproduces many of the expected features of the tidal currents in the region is produced. The sensitivity of the model to the amount of input data is critical. Confidence is gained when models run with independent data sets reveal similar features and characteristics. The error of the method can be determined using a bootstrap-type error analysis. It can be dangerous to model tides with small data sets in complex regions, although if the technique is used solely to estimate the mean flow fields smaller data sets may be acceptable.

Acknowledgements

We thank Julio Candela for early assistance and MATLAB code for running his tidal model. Leslie Rosenfeld and Steve Ramp provided significant contributions to our theoretical discussions on methods to remove tidal variance from ADCP data. Paul Jessen, Tarry Rago, and Heather Parker processed the ADCP data used in this study. Discussions with John Largier were helpful, and he and Steve Costa supplied the current meter data from CH2M Hill. Kaye Kinoshita processed and furnished the SSE current meter data. Dan Larson and the Scripps Data Zoo were the source for CCCCS current meter data, and Joe Bottero resurrected the SuperCODE mooring data. Barbara Hickey shared her data from the RP3 mooring. Funding for the SSE was provided by the EPA and the Naval Facilities Engineering Command, Western Division. Efforts of the master and crew of the *R/V Pt. Sur* and the officers and crew of

Table 2
Known current meter moorings in the Gulf of the Farallones. Data for each meter except those on the 1975 and 1977 EPA moorings have been located and found to be usable. Locations of the moorings are shown in Fig. 1.

Experiment	Mooring	Location	Depth	Dates
Hickey[a]	RP3	37.878N 122.623W	10 m	11/13/92–2/25/93
Slope/Shelf Experiment[b]	A	37.545N 122.854W	10 m 50 m 80 m	3/8/91–5/17/91; 7/14/91–1/5/92 3/8/91–5/17/91; 7/4/91–2/8/91 3/8/91–8/13/91
	B	37.477N 122.996W	10 m 150 m 260 m 390 m	7/4/91–9/23/91 3/9/91–2/8/92 3/9/91–2/8/92 3/9/91–2/8/92
	C	37.422N 123.135W	10 m 75 m 150 m 250 m 400 m 790 m	3/9/91–5/17/91; 7/4/91–2/8/92 3/9/91–3/21/91; 7/5/91–2/8/92 3/9/91–8/13/91 3/9/91–8/13/91 3/9/91–3/18/91; 8/14/91–9/10/91 3/9/91–3/30/91; 8/14/91–3/11/92
	D	37.364N 123.267W	75 m 250 m 400 m 800 m 1390 m	3/10/91–5/21/91; 7/5/91–2/13/92 3/10/91–9/3/91 3/10/91–2/13/91 3/10/91–6/11/91; 8/1/91–2/13/92 8/14/91–2/13/92
	E	37.640N 123.300W	75 m 250 m 400 m 800 m 1400 m 1987 m	3/11/91–4/16/91 3/11/91–8/15/91 3/11/91–2/12/92 3/11/91–2/12/92 3/11/91–2/12/92 3/11/91–2/12/92
	F	37.700N 123.144W	75 m 150 m 250 m 387 m	3/11/91–4/4/91; 8/15/91–2/10/92 3/12/91–2/13/92 3/11/91–2/13/92 3/11/91–2/13/92
USGS/Corps of Engineers[c]	346	37.635N 123.352W	200 m 400 m 800 m	7/7/90–8/21/90 7/7/90–8/21/90 7/7/90–8/21/90
	334	37.686N 122.796W	30 m 49 m	5/5/89–10/13/89 5/5/89–10/11/89
	335	37.784N 122.933W	30 m 59 m	5/5/89–10/13/89 5/5/89–10/10/89
Corps of Engineers[d]	1M	37.647N 122.700W	21 m 40 m	5/8/88–6/7/88; 1/30/89–5/27/89 5/8/89–5/27/89
	B1B	37.468N 122.786W	21 m 46 m 85 m	4/27/88–1/20/89 4/27/88–6/2/89 4/27/88–1/20/89
CH2M Hill[e]	A	37.705N 122.584W	8 m	6/19/87–8/2/87; 8/17/87–8/19/87 9/25/87–4/21/88; 5/9/88–7/18/88

Table 2. Continued.

Experiment	Mooring	Location	Depth	Dates
			14 m	6/19/87–7/27/87; 8/17/87–9/9/87 9/24/87–11/06/87; 11/18/87– 4/21/88 5/9/88–7/18/88
			20 m	6/19/87–7/26/87; 8/17/87–8/19/87 9/24/87–4/21/88; 5/9/88–7/18/88
	B	37.705N 122.547W	8 m 14 m	9/26/87–10/28/87; 4/27/88–6/3/88 4/27/88–6/3/88
	C	37.704N 122.517W	8 m	9/26/87–10/28/87; 4/27/88–6/3/88
	D	37.748N 122.555W	8 m	9/25/87–10/28/87; 4/27/88–6/3/88
	E	37.788N 122.527W	8 m 14 m 20 m	9/25/87–10/28/87; 4/26/88–6/4/88 9/25/87–10/28/87; 4/26/88–6/4/88 9/25/87–10/28/87; 4/26/88–6/4/88
	F	37.725N 122.605W	8 m 14 m	4/26/88–6/3/88 4/26/88–6/3/88
CCCCS[f]	K	37.289W 122.668W	70 m	2/14/84–2/3/85
	L	37.173N 122.926W	70 m 210 m 470 m	2/14/84–1/25/85 2/14/84–1/25/85 2/20/84–10/17/84
SuperCODE[g]	H3	37.370N 122.650W	35 m 65 m	4/22/81–3/10/82; 5/23/82–9/11/82 4/22/81–9/11/82
	H4	37.370N 122.850W	38 m 70 m 110 m	5/8/81–6/4/81 5/8/81–6/4/81 5/8/81–6/4/81; 8/16/81–3/6/82
EPA 1977[h]	2920	37.610N 123.126W	911 m	10/25/77–3/15/78
	2830 VACM	37.614N 123.246W	912 m 911 m	10/25/77–2/6/78 10/25/77–10/24/78
	2918 2919	37.614N 123.291W	1800 m 1829 m	10/25/77–12/21/77 10/25/77–3/10/78
EPA 1975[i]	1009	37.625N 123.283W	1729 m	8/21/75–9/17/75
	1028	37.642N 123.300W	1849 m	8/22/75–9/17/75

[a]Personal communication with Barbara Hickey.
[b]Ref.: Kinoshita et al. (1992).
[c]Ref.: Noble and Gelfenbaum (1991).
[d]Ref.: Sherwood et al. (1989).
[e]Ref.: CH2M Hill (1989).
[f]Ref.: Bratkovich et al. (1991).
[g]Ref.: Denbo et al. (1984).
[h]Ref.: Crabbs (1983) which references Interstate Electronics Corp (1982) as primary source.
[i]Ref.: Crabbs (1983) which references unpub material from R. Schwartzlose of SIO as primary source.

the NOAA Ship DAVID STARR JORDAN are gratefully acknowledged. Three anonymous but conscientious reviewers provided many constructive insights, suggestions, and comments. JS thanks the NOAA Corps and the leadership at the NOAA Pacific Fisheries Environmental Laboratory for the opportunity to pursue this study.

Appendix A. Current meters in the Gulf of the Farallones

To provide a resource for further studies in the Gulf of the Farallones, a listing of all known current meters moorings deployed in the region is included (Table 2). In addition to these meters, a large number of moorings which are not listed have been deployed within the Golden Gate and inside San Francisco Bay.

For all available current meter time series (except those on the 1975 and 1977 EPA moorings), the tidal ellipse characteristics have calculated for the M_2, S_2, K_1, and O_1 constituents (Tables 3–6) and plotted as the magnitudes and orientations of the semi-major axes (Fig. 2).

Appendix B. Constructing and using the model

For m observations of velocity and n tidal frequencies, an m by $8n + 4$ matrix **A** is created. The ith row of matrix **A** consists of the longitude, latitude, and depth of the ith observation (to solve for the steady current) and then the same multiplied by the periodic constituents for each frequency:

$$
\begin{aligned}
&[1\ \lambda_i\ \phi_i\ z_i \cos(2\pi\omega_1 t_i)\ \lambda \cos(2\pi\omega_1 t_i)\ \phi \cos(2\pi\omega_1 t_i)\ z \cos(2\pi\omega_1 t_i) \ \ldots \\
&\quad \sin(2\pi\omega_1 t_i)\ \lambda \sin(2\pi\omega_1 t_i)\ \phi \sin(2\pi\omega_1 t_i)\ z \sin(2\pi\omega_1 t_i) \ \ldots \\
&\quad \cos(2\pi\omega_2 t_i)\ \lambda \cos(2\pi\omega_2 t_i)\ \phi \cos(2\pi\omega_2 t_i)\ z \cos(2\pi\omega_2 t_i) \ \ldots \\
&\quad \sin(2\pi\omega_2 t_i)\ \lambda \sin(2\pi\omega_2 t_i)\ \phi \sin(2\pi\omega_2 t_i)\ z \sin(2\pi\omega_2 t_i) \ \ldots \qquad \text{(B.1)} \\
&\qquad\qquad \vdots \\
&\quad \cos(2\pi\omega_n t_i)\ \lambda \cos(2\pi\omega_n t_i)\ \phi \cos(2\pi\omega_n t_i)\ z \cos(2\pi\omega_n t_i) \ \ldots \\
&\quad \sin(2\pi\omega_n t_i)\ \lambda \sin(2\pi\omega_n t_i)\ \phi \sin(2\pi\omega_n t_i)\ z \sin(2\pi\omega_n t_i)].
\end{aligned}
$$

Column vectors b_u and b_v of m length are created where each element is the u or v velocity observed. The over-determined least-squares problems $\mathbf{A}c_u = b_u$ and $\mathbf{A}c_v = b_v$ are solved for column vectors c_u and c_v by finding the pseudoinverse of **A**. Each c_u and c_v has $8n + 4$ elements. The first four elements in c_u and c_v correspond to

Table 3
Ellipse characteristics for the M_2 tide calculated for each current meter deployed in the Gulf of the Farallones since 1981. Inclination is the bearing of the semi-major axis as measured counterclockwise from east (090°). Phase is the time in hours since 00:00 January 1, 1980 that the tide is oriented with the semi-major axis, divided by the tidal frequency (12.42 h), multiplied by 360°, and finally truncated to fall within 0–360°.

Station name and depth	Semi-major axis (cm/s)	Semi-minor axis (cm/s)	Inclination (deg fm E)	Phase (deg)	Station name and depth	Semi-major axis (cm/s)	Semi-minor axis (cm/s)	Inclination (deg fm E)	Phase (deg)
Hickey RP1 10 m	10.9	0.5	346.9	104.4	USGS/COE 335 59 m	3.1	1.4	30.5	63.5
SSE A 10 m	5.7	0.9	55.2	61.9	USGS/COE 346 200 m	4.0	0.1	156.3	130.5
SSE A 50 m	4.0	1.4	97.1	116.3	USGS/COE 346 400 m	2.7	1.4	73.4	60.7
SSE A 80 m	4.1	1.2	84.0	91.5	USGS/COE 346 800 m	4.3	−1.9	161.4	134.1
SSE B 10 m	1.0	−0.6	153.5	145.5	COE 1M 21 m	7.5	0.3	76.2	82.2
SSE B 150 m	4.1	0.2	82.9	101.7	COE 1M 40 m	5.9	1.5	67.5	67.9
SSE B 260 m	4.3	0.6	111.3	85.3	COE B1B 21 m	3.4	2.8	166.1	158.0
SSE B 390 m	4.1	0.5	109.8	137.2	COE B1B 46 m	4.3	1.2	104.7	105.2
SSE C 10 m	3.1	1.2	104.2	129.7	COE B1B 85 m	4.5	0.3	96.3	121.7
SSE C 75 m	4.0	0.0	80.8	123.6	CH2M Hill A 8 m	17.2	−3.0	88.3	108.0
SSE C 150 m	4.2	−0.1	75.6	102.2	CH2M Hill A 14 m	17.4	−2.6	78.3	91.3
SSE C 250 m	4.6	−0.4	76.2	102.3	CH2M Hill A 20 m	16.4	0.4	69.1	74.6
SSE C 400 m	6.4	−1.9	95.9	109.0	CH2M Hill B 8 m	22.0	−1.6	92.5	110.7
SSE C 790 m	8.7	−3.0	105.9	131.6	CH2M Hill B 14 m	4.0	−0.5	58.6	92.0
SSE D 75 m	4.2	−0.4	116.2	144.2	CH2M Hill C 8 m	21.1	0.4	112.7	88.3
SSE D 250 m	2.3	1.2	113.6	188.2	CH2M Hill D 8 m	33.9	−1.2	79.3	104.2
SSE D 400 m	2.7	0.5	101.5	127.8	CH2M Hill E 8 m	71.7	−6.4	70.0	126.9
SSE D 800 m	5.1	−1.2	93.2	85.9	CH2M Hill E 14 m	58.6	−0.5	72.8	126.4
SSE D 1390 m	5.1	0.5	116.6	93.6	CH2M Hill E 20 m	41.2	4.6	75.4	124.8
SSE E 75 m	2.7	−1.7	137.0	333.0	CH2M Hill F 8 m	25.7	−4.9	69.9	105.4
SSE E 250 m	2.5	1.0	50.7	85.1	CH2M Hill F 14 m	19.6	−0.1	59.4	85.2
SSE E 400 m	2.4	1.6	84.9	84.0	CCCCS K 70 m	9.6	−1.3	84.9	119.4
SSE E 800 m	3.7	−1.1	138.6	145.7	CCCCS L 70 m	10.5	−5.6	100.9	313.4
SSE E 1400 m	2.2	−0.5	107.2	99.2	CCCCS L 210 m	6.1	−1.2	94.6	122.1
SSE F 75 m	2.5	0.1	24.6	51.3	CCCCS L 470 m	4.9	−0.4	94.6	227.3
SSE F 150 m	2.2	0.2	164.2	164.5	SuperCODE H3 35 m	8.8	−0.2	100.5	76.7
SSE F 250 m	1.1	0.3	141.6	96.8	SuperCODE H3 65 m	7.5	0.8	91.8	94.2
SSE F 387 m	0.8	0.1	69.1	332.5	SuperCODE H4 38 m	13.7	−4.0	133.8	116.3
USGS/COE 334 30 m	6.0	1.1	80.8	109.7	SuperCODE H4 70 m	9.8	−0.5	139.1	125.0
USGS/COE 334 49 m	6.0	1.2	66.1	94.3	SuperCODE H4 110 m	4.9	2.0	109.9	119.3
USGS/COE 335 30 m	3.3	1.3	26.5	61.1					

Table 4
Ellipse characteristics for the S_2 tide calculated for each current meter deployed in the Gulf of the Farallones since 1981. Inclination is the bearing of the semi-major axis as measured counterclockwise from east (090°). Phase is the time in hours since 00:00 January 1, 1980 that the tide is oriented with the semi-major axis, divided by the tidal frequency (12.00 h), multiplied by 360°, and finally truncated to fall within 0–360°.

Station name and depth	Semi-major axis (cm/s)	Semi-minor axis (cm/s)	Inclination (deg fm E)	Phase (deg)	Station name and depth	Semi-major axis (cm/s)	Semi-minor axis (cm/s)	Inclination (deg fm E)	Phase (deg)
Hickey RP1 10 m	1.9	0.0	165.8	351.9	USGS/COE 335 59 m	1.2	0.3	163.4	252.7
SSE A 10 m	2.2	0.8	58.9	124.5	USGS/COE 346 200 m	0.7	0.2	160.5	250.8
SSE A 50 m	1.6	−0.1	137.0	194.1	USGS/COE 346 400 m	1.3	0.0	70.0	156.3
SSE A 80 m	2.1	0.0	141.1	9.2	USGS/COE 346 800 m	1.4	−0.6	157.5	213.7
SSE B 10 m	2.2	−1.1	129.0	221.2	COE 1M 21 m	2.4	0.5	88.7	146.1
SSE B 150 m	1.5	−0.2	103.2	168.2	COE 1M 40 m	1.6	0.8	70.6	122.1
SSE B 260 m	1.5	0.5	134.5	164.7	COE B1B 21 m	1.5	1.0	168.7	228.4
SSE B 390 m	4.8	−0.3	136.8	191.7	COE B1B 46 m	1.8	0.2	131.8	186.5
SSE C 10 m	1.6	0.2	92.1	220.8	COE B1B 85 m	1.7	−0.3	119.6	193.0
SSE C 75 m	3.7	−1.5	61.1	197.5	CH2M Hill A 8 m	4.8	−0.6	93.2	157.1
SSE C 150 m	2.4	−1.5	78.2	199.5	CH2M Hill A 14 m	5.7	−0.1	84.1	137.6
SSE C 250 m	1.5	−1.1	98.9	181.9	CH2M Hill A 20 m	4.0	0.8	78.0	114.1
SSE C 400 m	2.3	−1.0	89.3	206.7	CH2M Hill B 8 m	5.3	0.0	94.4	149.3
SSE C 790 m	5.1	−2.3	129.0	222.8	CH2M Hill B 14 m	2.5	0.7	166.8	325.5
SSE D 75 m	1.4	−0.2	109.6	218.9	CH2M Hill C 8 m	4.9	0.7	114.9	142.3
SSE D 250 m	1.1	0.0	70.5	170.6	CH2M Hill D 8 m	7.9	−0.1	87.3	155.0
SSE D 400 m	1.0	−0.3	67.5	176.5	CH2M Hill E 8 m	17.3	−0.5	69.3	167.4
SSE D 800 m	2.5	−0.9	107.6	165.3	CH2M Hill E 14 m	13.9	−1.4	67.1	166.7
SSE D 1390 m	2.9	−0.1	118.7	171.5	CH2M Hill E 20 m	9.5	−1.4	65.2	160.2
SSE E 75 m	2.9	−0.7	140.0	120.9	CH2M Hill F 8 m	4.1	0.0	81.3	153.2
SSE E 250 m	1.0	0.0	33.1	152.2	CH2M Hill F 14 m	2.6	0.6	50.9	117.8
SSE E 400 m	1.1	0.2	108.6	186.9	CCCCS K 70 m	4.5	−0.8	113.5	178.7
SSE E 800 m	1.2	−0.2	142.0	211.9	CCCCS L 70 m	3.4	−1.9	98.6	24.5
SSE E 1400 m	1.0	−0.2	123.6	156.3	CCCCS L 210 m	2.6	−0.9	98.4	1.1
SSE F 75 m	1.4	−0.4	174.9	298.2	CCCCS L 470 m	1.3	0.7	125.5	145.1
SSE F 150 m	0.6	0.1	0.8	52.6	SuperCODE H3 35 m	2.5	0.1	113.0	145.4
SSE F 250 m	0.5	0.0	148.3	171.6	SuperCODE H3 65 m	2.5	−0.1	88.4	165.0
SSE F 387 m	0.4	0.0	72.2	86.0	SuperCODE H4 38 m	3.6	−2.2	45.9	150.6
USGS/COE 334 30 m	1.5	0.7	120.6	205.7	SuperCODE H4 70 m	2.5	−1.4	105.4	168.5
USGS/COE 334 49 m	1.5	0.5	105.7	189.4	SuperCODE H4 110 m	2.8	−1.2	129.0	185.5
USGS/COE 335 30 m	1.3	0.4	14.0	98.1					

Table 5
Ellipse characteristics for the K_1 tide calculated for each current meter deployed in the Gulf of the Farallones since 1981. Inclination is the bearing of the semi-major axis as measured counterclockwise from east (090°). Phase is the time in hours since 00 : 00 January 1, 1980 that the tide is oriented with the major axis, divided by the tidal frequency (23.93 h), multiplied by 360°, and finally truncated to fall within 0–360°.

Station name and depth	Semi-major axis (cm/s)	Semi-minor axis (cm/s)	Inclination (deg fm E)	Phase (deg)	Station name and depth	Semi-major axis (cm/s)	Semi-minor axis (cm/s)	Inclination (deg fm E)	Phase (deg)
Hickey RP1 10 m	5.4	1.1	176.3	6.5	USGS/COE 335 59 m	5.7	−1.0	134.3	185.5
SSE A 10 m	5.3	−2.7	75.3	106.2	USGS/COE 346 200 m	2.3	0.1	150.9	206.6
SSE A 50 m	6.1	−3.3	88.6	112.6	USGS/COE 346 400 m	2.1	−0.1	148.4	209.8
SSE A 80 m	6.2	−2.2	125.0	143.3	USGS/COE 346 800 m	1.8	−0.5	149.7	194.3
SSE B 10 m	1.3	−0.8	88.2	143.3	COE 1M 21 m	8.2	−2.9	88.3	113.6
SSE B 150 m	2.8	−0.3	88.9	150.8	COE 1M 40 m	4.5	0.0	120.6	134.2
SSE B 260 m	2.0	−0.4	107.8	152.5	COE B1B 21 m	6.0	−2.3	83.7	113.8
SSE B 390 m	1.4	−0.4	133.4	165.8	COE B1B 46 m	6.8	−3.5	84.1	115.6
SSE C 10 m	0.7	0.0	53.7	310.7	COE B1B 85 m	4.4	−1.4	126.2	145.1
SSE C 75 m	1.7	−1.0	104.4	205.6	CH2M Hill A 8 m	9.6	−5.7	97.5	103.4
SSE C 150 m	2.8	−0.5	95.8	157.1	CH2M Hill A 14 m	6.3	0.6	106.6	98.5
SSE C 250 m	2.1	−0.2	91.9	157.0	CH2M Hill A 20 m	7.0	3.3	137.0	131.7
SSE C 400 m	1.3	0.3	70.6	172.8	CH2M Hill B 8 m	8.7	−2.3	101.8	99.7
SSE C 790 m	6.4	−1.8	78.6	155.5	CH2M Hill B 14 m	2.7	0.2	16.9	20.9
SSE D 75 m	2.0	−0.1	110.6	158.6	CH2M Hill C 8 m	7.6	−0.3	117.1	67.4
SSE D 250 m	1.8	0.0	101.8	162.2	CH2M Hill D 8 m	12.7	−3.5	86.1	122.5
SSE D 400 m	1.7	0.1	87.5	168.3	CH2M Hill E 8 m	24.3	−2.5	71.5	145.6
SSE D 800 m	2.0	−0.2	68.2	151.3	CH2M Hill E 14 m	20.1	−4.1	66.1	147.4
SSE D 1390 m	1.5	−1.2	129.8	147.0	CH2M Hill E 20 m	15.3	−2.7	57.3	154.7
SSE E 75 m	2.3	−1.3	177.1	313.9	CH2M Hill F 8 m	15.3	−7.6	82.5	116.1
SSE E 250 m	2.2	0.2	116.6	202.5	CH2M Hill F 14 m	8.6	−0.1	105.2	120.7
SSE E 400 m	1.9	0.1	119.2	194.0	CCCCS K 70 m	7.1	−2.7	62.0	85.0
SSE E 800 m	1.1	−0.2	121.8	179.6	CCCCS L 70 m	2.0	−0.2	48.0	30.2
SSE E 1400 m	1.5	−1.0	2.3	298.1	CCCCS L 210 m	2.2	0.2	85.4	51.9
SSE F 75 m	3.3	−1.0	114.3	147.6	CCCCS L 470 m	3.3	0.4	97.7	110.8
SSE F 150 m	4.2	0.1	121.3	177.0	SuperCODE H3 35 m	6.4	−2.5	79.6	89.8
SSE F 250 m	2.6	0.2	124.8	168.3	SuperCODE H3 65 m	4.9	−1.4	95.9	105.9
SSE F 387 m	0.3	0.0	170.9	106.6	SuperCODE H4 38 m	5.9	−2.2	69.2	119.4
USGS/COE 334 30 m	8.4	−3.4	100.9	150.9	SuperCODE H4 70 m	7.3	−1.0	72.0	123.6
USGS/COE 334 49 m	6.5	−1.5	122.2	166.2	SuperCODE H4 110 m	6.1	−3.3	70.1	119.7
USGS/COE 335 30 m	7.5	−2.8	112.1	160.9					

Table 6
Ellipse characteristics for the O_1 tide calculated for each current meter deployed in the Gulf of the Farallones since 1981. Inclination is the bearing of the semi-major axis as measured counterclockwise from east (090°). Phase is the time in hours since 00:00 January 1, 1980 that the tide is oriented with the semi-major axis, divided by the tidal frequency (25.82 h), multiplied by 360°, and finally truncated to fall within 0–360°.

Station name and depth	Semi-major axis (cm/s)	Semi-minor axis (cm/s)	Inclination (deg fm E)	Phase (deg)	Station name and depth	Semi-major axis (cm/s)	Semi-minor axis (cm/s)	Inclination (deg fm E)	Phase (deg)
Hickey RP1 10 m	3.3	0.6	175.1	314.5	USGS/COE 335 59 m	3.4	−0.8	127.5	109.5
SSE A 10 m	2.7	−1.4	69.5	79.5	USGS/COE 346 200 m	1.7	0.0	145.9	162.6
SSE A 50 m	3.1	−1.6	79.7	72.5	USGS/COE 346 400 m	1.3	0.2	138.2	168.7
SSE A 80 m	3.0	−1.3	111.8	89.1	USGS/COE 346 800 m	1.0	−0.2	161.6	183.7
SSE B 10 m	0.6	0.1	171.4	99.7	COE 1M 21 m	5.4	−2.6	86.0	65.1
SSE B 150 m	1.3	0.0	83.0	115.3	COE 1M 40 m	2.8	−0.4	109.0	75.9
SSE B 260 m	0.9	−0.1	117.3	122.8	COE B1B 21 m	3.4	−1.7	79.5	58.0
SSE B 390 m	0.8	0.0	117.5	137.6	COE B1B 46 m	3.8	−1.8	76.6	52.9
SSE C 10 m	0.7	−0.4	10.9	0.8	COE B1B 85 m	2.6	−1.0	112.7	76.5
SSE C 75 m	0.9	0.3	115.8	101.9	CH2M Hill A 8 m	5.3	−3.8	95.0	70.3
SSE C 150 m	1.4	0.3	97.7	138.3	CH2M Hill A 14 m	3.9	−0.2	92.5	45.8
SSE C 250 m	1.0	0.2	73.4	109.8	CH2M Hill A 20 m	2.7	1.9	167.5	121.1
SSE C 400 m	1.2	0.0	92.9	144.7	CH2M Hill B 8 m	5.4	−1.9	101.3	69.1
SSE C 790 m	4.0	−1.0	80.8	115.3	CH2M Hill B 14 m	2.5	−1.0	102.3	338.6
SSE D 75 m	1.0	0.1	89.3	118.7	CH2M Hill C 8 m	6.0	0.2	118.5	28.7
SSE D 250 m	1.0	0.3	92.8	120.7	CH2M Hill D 8 m	7.9	−3.4	85.9	101.4
SSE D 400 m	1.1	0.1	82.6	135.1	CH2M Hill E 8 m	15.6	−1.1	70.3	117.3
SSE D 800 m	1.3	0.0	73.2	129.9	CH2M Hill E 14 m	13.8	−3.3	59.5	121.7
SSE D 1390 m	1.1	−0.6	103.1	130.7	CH2M Hill E 20 m	11.6	−3.5	50.7	128.0
SSE E 75 m	2.0	0.5	132.6	303.3	CH2M Hill F 8 m	8.9	−6.4	94.3	73.4
SSE E 250 m	1.4	0.3	113.2	169.0	CH2M Hill F 14 m	4.8	−0.5	91.3	61.2
SSE E 400 m	1.3	0.2	122.7	167.7	CCCCS K 70 m	3.7	−1.0	46.5	15.6
SSE E 800 m	0.8	−0.1	123.3	163.4	CCCCS L 70 m	1.1	0.0	53.9	336.1
SSE E 1400 m	0.8	−0.6	25.2	240.7	CCCCS L 210 m	1.1	0.1	60.4	334.0
SSE F 75 m	2.4	−1.0	105.1	114.0	CCCCS L 470 m	1.6	0.2	100.4	236.3
SSE F 150 m	2.9	0.0	122.5	142.1	SuperCODE H3 35 m	2.7	−1.5	71.4	357.8
SSE F 250 m	1.7	0.1	125.3	128.4	SuperCODE H3 65 m	1.9	−0.8	86.8	15.6
SSE F 387 m	0.3	0.0	166.5	55.0	SuperCODE H4 38 m	2.5	−0.7	108.7	63.0
USGS/COE 334 30 m	4.4	−2.6	91.7	977.1	SuperCODE H4 70 m	3.2	−1.5	96.4	35.0
USGS/COE 334 49 m	3.8	−1.8	112.1	105.4	SuperCODE H4 110 m	2.2	−1.4	62.4	39.9
USGS/COE 335 30 m	4.4	−1.7	104.6	94.3					

the mean flow, followed by n sets of eight elements. The elements of each set correspond to the coefficients a–h in Eq. (3). Thus,

$$u_0(\lambda, \phi, z) = c_u(1) + c_u(2)\lambda + c_u(3)\phi + c_u(4)z,$$
$$v_0(\lambda, \phi, z) = c_v(1) + c_v(2)\lambda + c_v(3)\phi + c_v(4)z, \tag{B.2}$$

and at any time t the u and v tidal velocities at λ, ϕ, z, for frequency ω_k is

$$u(\lambda, \phi, z, t) = A_1 \cos(2\pi\omega_k t) + B_1 \sin(2\pi\omega_k t),$$
$$v(\lambda, \phi, z, t) = A_2 \cos(2\pi\omega_k t) + B_2 \sin(2\pi\omega_k t), \tag{B.3}$$

where

$$A_1 = c_u(8k-3) + c_u(8k-2)\lambda + c_u(8k-1)\phi + c_u(8k)z,$$
$$B_1 = c_u(8k+1) + c_u(8k+2)\lambda + c_u(8k+3)\phi + c_u(8k+4)z,$$
$$A_2 = c_v(8k-3) + c_v(8k-2)\lambda + c_v(8k-1)\phi + c_v(8k)z \tag{B.4}$$
$$B_2 = c_v(8k+1) + c_v(8k+2)\lambda + c_v(8k+3)\phi + c_v(8k+4)z.$$

However, tidal currents are in many ways easier to express as the sum of clockwise and counterclockwise rotating vectors (Godin, 1972), $\boldsymbol{U} = u + \mathrm{i}v = U_+ \mathrm{e}^{i\omega t} + U_- \mathrm{e}^{-i\omega t}$. Here, $\mathrm{e}^{i\omega t}$ and $\mathrm{e}^{-i\omega t}$ are unit vectors rotating in opposite directions and U_+ and U_- are complex quantities representing the vector magnitudes.

$$|U_+| = \tfrac{1}{2}[(A_1 + B_2)^2 + (A_2 - B_1)^2]^{1/2},$$
$$|U_-| = \tfrac{1}{2}[(A_1 - B_2)^2 + (A_2 + B_1)^2]^{1/2}. \tag{B.5}$$

Furthermore, the length of the ellipse axes are

$$\text{major axis} = |U_+| + |U_-|,$$
$$\text{minor axis} = |U_+| - |U_-|. \tag{B.6}$$

The sign of the semi-minor axis gives the sense of the tides rotation; positive means counterclockwise and negative means clockwise. The orientation of the semi-major axis with respect to east is

$$\theta = \tfrac{1}{2}\tan^{-1}\left[\frac{2(A_1A_2 + B_1B_2)}{A_1^2 + B_1^2 - A_2^2 - B_2^2}\right] \tag{B.7}$$

and the phase with respect to the semi-major axis is

$$\tau = \tfrac{1}{2}\tan^{-1}\left[\frac{2(A_1B_1 + A_2B_2)}{A_1^2 - B_2^2 + A_2^2 - B_1^2}\right]. \tag{B.8}$$

References

Allen, J.T., 1995. Subtidal and tidal currents in the vicinity of the Iceland-Færœs front. Journal of Atmospheric and Oceanic Technology 12, 567–588.

Bratkovich, A., Bernstein, R.L., Chelton, D.B., Kosro, P.M., 1991. Central California coastal circulation study: program overview and representative results, in Southern California Bight Physical Oceanography. Proceedings of a Workshop. OCS Study MMS 91-0033, pp. 91–109.

Candela J., Beardsley, R.C., Limeburner, R. Removing tides from ship-mounted ADCP data, with application to the Yellow Sea (1990). In: Appell, G.F., Curtin, T.B. (Eds) Proceedings of the IEEE Fourth Working Conference on Current Measurements. Institute of Electrical and Electronics Engineers, New York, pp. 258–266.

Candela, J., Beardsley, R.C., Limeburner, R., 1992. Separation of tidal and subtidal currents in ship-mounted acoustic doppler current profiler observations. Journal of Geophysical Research 97, 769–788.

Cartwright, D.E., Ray, R.D., 1991. Energetics of global ocean tides from Geosat altimetry, Journal of Geophysical Research 96, 16 897–16 912.

CH2M Hill, 1989. Wastewater transport and bacteriological compliance studies of the San Francisco ocean outfall. City and County of San Francisco.

Chelton, D.B., Bernstein, R.L., Bratkovich, A., Kosro, P.M., 1987. The central California coastal circulation study. EOS Transactions AGU 68(1), 12–13.

Chelton, D. B., Bratkovich, A.W., Bernstein, R.L., Kosro, P.M., 1988. Poleward flow off central California during the Spring and Summer of 1981 and 1984. Journal of Geophysical Research 93, 10 604–10 620.

Collins, C.A., Paquette, R.G., Ramp, S.R., 1996. Annual variability of ocean currents at 350-m depth over the continental slope of Point Sur, California. California Cooperative Oceanic Fisheries Investigation Report 37, 257–263.

Crabbs, D.E., 1983. Analysis of ocean current meter records obtained from a 1975 deployment off the Farallon Islands, California. Interstate Electronics Corp., Anaheim, CA.

Denbo, D.W., Polzin, K., Allen, J.S., Huyer, A., Smith, R.L., 1984. Current meter observations over the continental shelf off Oregon and California. February 1981–January 1984, Data Report 112, Oregon State University.

Dowd, M., Thompson, K.R., 1996. Extraction of tidal streams from ship-bourne acoustic Doppler current profiler using a statistical-dynamical model. Journal of Geophysical Research 101, 8943–8956.

Egbert, G., Bennett, A.F., Foreman, M.G., 1994. Topex/Poseidon tides estimated using a global inverse model, Journal of Geophysical Research 99, 24 821–24 852.

Foreman, M.G.G., 1978. Tidal analysis program package. Pacific Marine Science Report 78-6, Institute of Ocean Sciences.

Foreman, M.G.G., Freeland, H.J., 1991. A comparison of techniques for tide removal from ship-mounted acoustic doppler measurements along the southwest coast of Vancouver Island. Journal of Geophysical Research 96, 17 007–17 021.

Geyer, W.R., Signell, R., 1990. Measurements of tidal flow around a headland with a shipboard acoustic doppler current profiler. Journal of Geophysical Research 95, 3189–3197.

Gezgin, E., 1991. A study on hydrographic conditions and salt budget calculation for the Gulf of the Farallones with the data collected in August 1990. M.S. Thesis, Naval Postgraduate School, Monterey, CA.

Godin, G.G., 1972. The Analysis of Tides. Univ. Of Toronto Press, Toronto, 264 pp.

Hendershott, M.C., 1973. Ocean tides. EOS Transactions AGU 54, 76–86.

Interstate Electronics Corporation, 1982. Farallon Islands Oceanographic Data Analysis, vols. I and II. Interstate Electronics Corp., Anaheim, CA.

Jessen, P.F., Ramp, S.R., Collins, C.A., Garfield, N., Rosenfeld, L.K., Schwing, F.B., 1992a. Hydrographic and acoustic doppler current profiler (ADCP) data from the Farallones shelf and slope study 13–18 February 1991. Naval Postgraduate School Technical Report NPS-OC-92-003, Monterey, CA.

Jessen, P.F., Ramp, S.R., Collins, C.A., Garfield, N., Rosenfeld, L.K., Schwing, F.B., 1992b. Hydrographic and acoustic doppler current profiler (ADCP) data from the Farallones shelf and slope study 16–21 May 1991. Naval Postgraduate School Technical Report NPS-OC-92-004, Monterey, CA.

Jessen, P.F., Ramp, S.R., Collins, C.A., Garfield. N., Rosenfeld, L.K., Schwing, F.B., 1992c. Hydrographic and acoustic doppler current profiler (ADCP) data from the Farallones shelf and slope study 29 October–3 November 1991. Naval Postgraduate School Technical Report NPS-OC-92-007, Monterey, CA.

Jessen, P.F., Ramp, S.R., Collins, C.A., Garfield, N., Rosenfeld, L.K., Schwing, F.B., 1992d. Hydrographic and acoustic doppler current profiler (ADCP) data from the Farallones shelf and slope study 7–17 February 1992. Naval Postgraduate School Technical Report NPS-OC-92-005, Monterey, CA.

Katoh, O., Teshima, K., Abe, O., Fujita, H., Miyaji, K., Moringa, K., Nakagawa, N., 1996. Process of Tsushima current formation revealed by ADCP measurements in summer. Journal of Oceanography 52, 491–507.

Kinoshita, K., Noble, M., Ramp, S.R., 1992. The Farallones Moored Array Data Report. USGS, Menlo Park, CA.

Kinsella, A., 1986. Numerical solutions for error evaluation, American Journal of Physics 54, 464–466.

Largier, J.L., 1996. Hydrodynamic exchange between San Francisco Bay and the ocean: the role of ocean circulation and stratification. In: Hollinbaugh, J.T. (Ed.), San Francisco Bay: the Ecosystem. American Association for the Advancement of Science, San Francisco, CA.

Mofjeld, H.O., Gonzalez, F.I., Eble, M.C., 1995. Ocean tides in the continental mar gin off the Pacific northwest shelf. Journal of Geophysical Research 100, 10 789–10 800.

Nelson, C.S., 1977. Wind stress and wind stress curl over the California current, U.S. Department of Commerce, NOAA Technical Report NMFS-SSRF-714.

Noble, M., Rosenfeld, L.K., Smith, R.L., Gardner, J.V., Beardsley, R.C., 1987. Tidal currents seaward of the northern California continental shelf. Journal of Geophysical Research 92, 1733–1744.

Noble, M., Gelfenbaum, G., 1990. A pilot study of currents and suspended sediment in the Gulf of the Farallones. USGS, Menlo Park, CA.

Parker, H.A., 1996. Variations in coastal circulation off central California, spring-summer of 1993, 1994, 1995. M.S. Thesis, Naval Postgraduate School, Monterey, CA.

Petruncio, E.T., 1996. Observations and modeling of the internal tide in a submarine canyon. Ph.D. Dissertation, Naval Postgraduate School, Monterey, CA.

Petzrick, E.P., Collins, C.A., Boicourt, W.C., 1996. Currents through the Golden Gate. In: Hollinbaugh, J.T. (Ed.), San Francisco Bay: the Ecosystem. American Association for the Advancement of Science, San Francisco, CA.

Prazuck, C., 1991. Anomalous diurnal currents in the vicinity of the Yermak Plateau. Ph.D. Dissertation, Naval Postgraduate School, Monterey, CA.

Rago, T.A., Rosenfeld, L.K., Jessen, P.F., Ramp, S.R., Collins, C.A., Garfield, N., Schwing, F.B., 1992. Hydrographic and acoustic doppler current profiler (ADCP) data from the Farallones shelf and slope study 12–18 August 1991. Naval Postgraduate School Technical Report NPS-OC-92-006, Monterey, CA.

Ramp, S.R., Garfield, N., Collins, C.A., Rosenfeld, L.K., Schwing, F., 1995. Circulation studies over the continental shelf and slope near the Farallon Islands. CA, Naval Postgraduate School Technical Report NPS-OC-95-004, Monterey, CA.

Rosenfeld, L.K., Beardsley, R.C., 1987. Barotropic semidiurnal tidal currents off northern California during the Coastal Ocean Dynamics Experiment (CODE). Journal of Geophysical Research 92, 1721–1732.

Schwing, F.B., O'Farrell, M., Steger, J., Baltz, K., 1996. Coastal upwelling indices, west coast of North America 1946–1995. NOAA Technical Report NOAA-TM-NMFS-SWFSC-231, US Department of Commerce.

Sherwood, C.R., Coats, D., Walls, B., 1989. Current and suspended sediment measurements on the Central California continental shelf. In: Proceedings of Oceans '89 Conference, IEEE Publication No. 89CH2780-5, pp. 320–325.

Steger, J.M., 1997. Use of ship-mounted acoustic Doppler current profiler data to study mesoscale oceanic circulation patterns in the Archipiélago de Colon (Galapagos Islands) and the Gulf of the Farallones. Ph.D. Dissertation, Naval Postgraduate School, Monterey, CA.

Steiner, M.T., 1994. Detiding shipboard-mounted ADCP data: an analysis of model data and observations using a polynomial interpolation method. M.S. Thesis, Naval Postgraduate School, Monterey, CA.

Strub, P.T., Allen, J.S., Huyer, A., Smith, R.L., 1987. Seasonal cycles of currents, temperatures, winds, and sea level over the northeast Pacific continental shelf: 35°N. to 48°N. Journal of Geophysical Research 92, 1507–1526.